AD-A148 255 MIZEX A PROGRAM FOR MESOSCALE AIR-ICE-OCEAN INTERACTION 1/1
EXPERIMENTS IN AR.. (U) COLD REGIONS RESEARCH AND
ENGINEERING LAB HANOVER NH M G MCPHEE ET AL. SEP 84
UNCLASSIFIED CRREL-SR-84-28 N00014-78-G-0052 F/G 8/12 NL

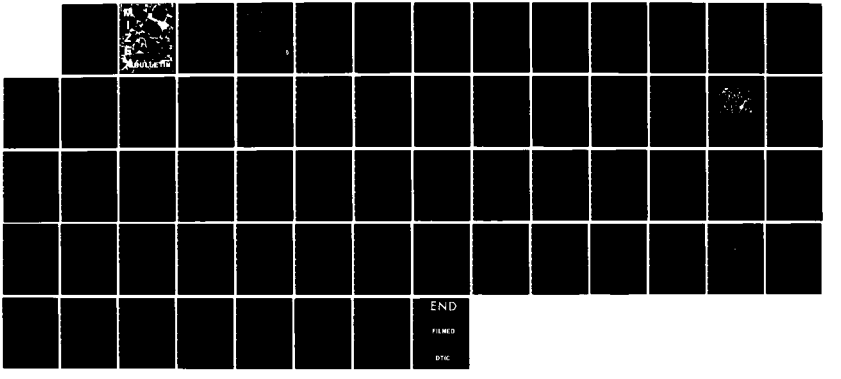

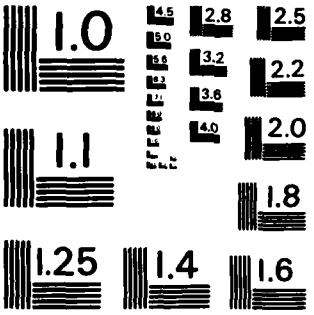

MICROCOPY RESOLUTION TEST CHART
NATIONAL BUREAU OF STANDARDS-1963-A

MIZEX

: INITIAL RESULTS AND ANALYSIS FROM MIZEX '83

SEPTEMBER 1984

BULLETIN

84

MIZEX BULLETIN SERIES: INFORMATION FOR CONTRIBUTORS

The main purpose of the MIZEX Bulletin series* is to provide a permanent medium for the interchange of initial results, data summaries, and theoretical ideas relevant to the Marginal Ice Zone Experiment. This series will be unrefereed and should not be considered a substitute for more complete and finalized journal articles.

Because of the similarity of the physics of the marginal ice zone in different regions, contributions relevant to any marginal ice zone are welcome, provided they are relevant to the overall goals of MIZEX.

These overall goals are discussed in Bulletin I (Wadhams et al., CRREL Special Report 81-19), which described the research strategy, and Bulletin II (Johannesen et al., CRREL Special Report 83-12), which outlined the science plan for the main 1984 summer experiment. Copies of earlier or current bulletins may be obtained from the Technical Information Branch, USA CRREL.

Persons interested in contributing articles to the bulletin should send copies to one of the editors listed below with figures reproducible in black and white. Proofs of the retyped manuscripts will not be sent to the author unless specifically requested.

Science Editors:

W.D. Hibler III
USA Cold Regions Research and
and Engineering Laboratory
72 Lyme Road
Hanover, New Hampshire 03755-1290

Peter Wadhams
Scott Polar Research Institute
Lensfield Road
Cambridge CB2 1ER
United Kingdom

Technical Editor:

Maria Bergstad
USA Cold Regions Research
and Engineering Laboratory
72 Lyme Road
Hanover, New Hampshire 03755-1290

* The MIZEX Bulletin series is funded by the Office of Naval Research.

Cover: The MV Polarbjørn *in the marginal ice zone during the drift phase. Photo taken 27 June 1983 from an altitude of 1400 ft by Vernon Squires. The* Polarbjørn *is 50 m in length.*

MIZEX
A Program for Mesoscale Air – Ice – Ocean Interaction Experiments in Arctic Marginal Ice Zones

IV: INITIAL RESULTS AND ANALYSIS FROM MIZEX 83

September 1984

U.S. Army Cold Regions Research and Engineering Laboratory
Hanover, New Hampshire, USA

CRREL Special Report 84-28

PREFACE

This bulletin contains initial results and analyses derived from the 1983 MIZEX pilot study in the Greenland-Norwegian Sea in June and July. While only a pilot study, this scientific expedition, carried out in three phases with two personnel exchanges, represented one of the most complete investigations of processes at a decaying ice edge to that date. Much of this data forms an independent and usable analysis for comparison with the 1984 main summer experiment. This report lists initial results from several of the experiments with special emphasis on sea ice dynamics and decay. Other analyses will appear in future bulletins.

CONTENTS

Drift Velocity During the Drift-Station Phase of MIZEX 83

MILES G. McPHEE
McPhee Research Co., Rte 8, Box 304H
Yakima, Washington 98908

A basic initial step in analyzing measurements of velocity taken relative to a drifting ice station is to determine the velocity of the station itself. During the drift-station phase of MIZEX 83, which started at about 0900 on day 179 and ended at 1200 on day 189, the M/V *Polarbjørn* was moored to adjacent ice floes and, except for very minor adjustments, its trajectory was exactly representative of those floes. The geographic location of the ship was monitored by satellite positioning, which furnished typically about 40 fixes per day, with accuracy somewhere in the neighborhood of 200 m.

This note describes a fitting technique developed for on-site, microprocessor analysis of station velocity to be implemented for the 1984 drift experiment, which will be of much longer duration. It is preliminary in the sense that neither a rigorous optimization of the fitted parameters nor a velocity error analysis has been carried out. Nevertheless, it presents a potentially useful technique that has not appeared elsewhere, and also provides a velocity synthesis that may be helpful for investigators who had fixed and profiling current measuring systems in the vicinity of the ice station. The appendix contains an hourly listing of the fitted velocity during the 10 days of the drift-station phase.

Suppose that over some period of time we can approximate an ice drift trajectory as a superposition of mean motion plus oscillations with preferred inertial and diurnal frequencies. Differences between the semidiurnal and inertial frequencies are considered unresolvable. The oscillating components are cyclical (i.e., a trajectory due to the oscillation alone returns to its initial value after one period), but not necessarily circular. The velocity is then:

$$V(t) = V_m + S_{cw}\, e^{-ift} + S_{ccw}\, e^{ift} + D_{cw}\, e^{-i\omega t} + D_{ccw}\, e^{i\omega t} \qquad (1)$$

where f is the angular frequency of the inertial (semidiurnal at high latitudes) oscillation with coefficients S_{cw} and S_{ccw}, the subscripts referring respectively to clockwise and counterclockwise rotation. D_{cw}, D_{ccw}, and ω similarly describe the diurnal oscillation.

The trajectory for an arbitrary time reference, $t_0 = 0$, with initial position X_0, is given, from integration of (1), by

$$X(t) = X_0 + V_m t + (i/f)\{S_{cw}(e^{-ift}-1) + S_{ccw}(1-e^{ift})\} + (i/\omega)\{D_{cw}(e^{-i\omega t}-1) + D_{ccw}(1-e^{i\omega t})\}. \qquad (2)$$

For illustration, consider a trajectory consisting of (a) mean motion to the ENE (60° bearing): $V_m = (8.66,5)$ cm s^{-1}; (b) a pure inertial oscillation with amplitude 10 cm s^{-1}: $V_f = (-10,0)\exp(-ift)$; and (c) a diurnal tidal ellipse: $V_\omega = (15,0)\exp(-i\omega t) + (0,5)\exp(i\omega t)$. Note that the rotary spectrum of such motion would show strong peaks in the clockwise spectrum at f and ω, with a weaker peak at ω only in the CCW spectrum. Figure 1 illustrates the two oscillating trajectories by themselves, and then the total trajectory over 48 hr, when they are superimposed on the steady mean drift. Note the scale changes in the sketch.

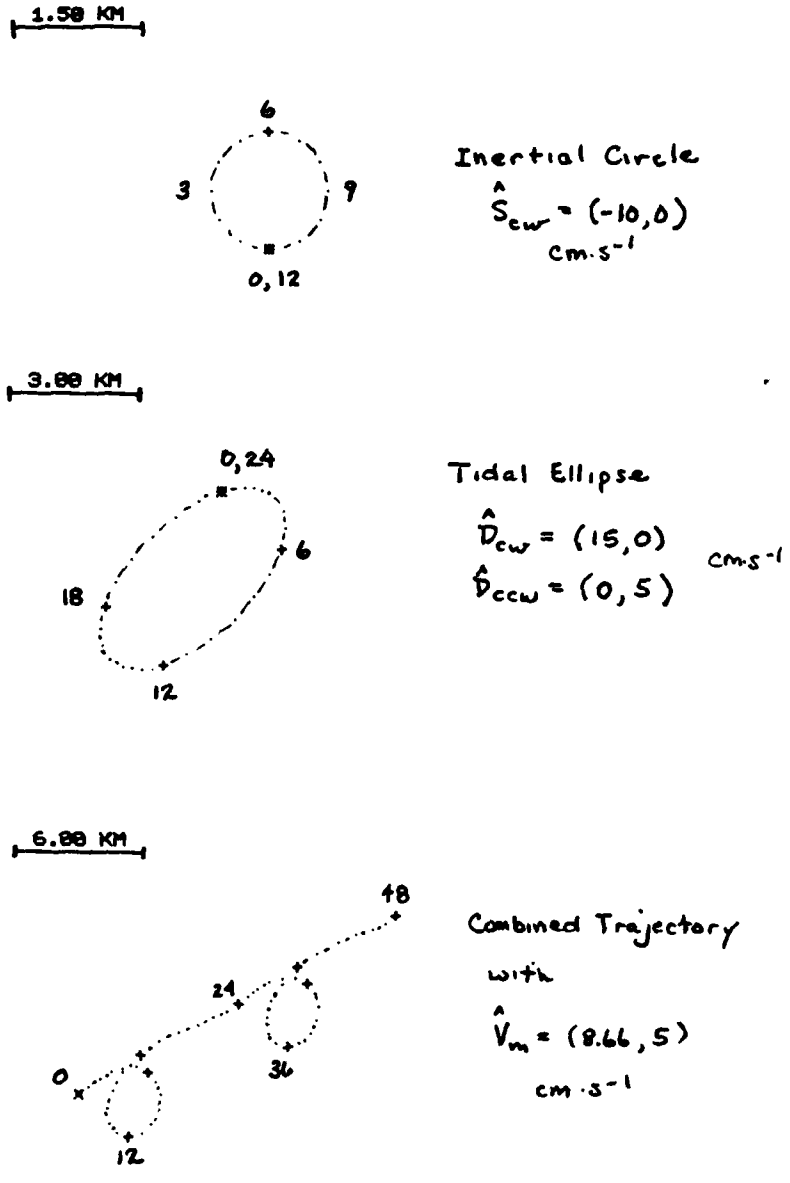

Fig. 1. Trajectories associated with a) a pure inertial oscillation with period 12 hr and velocity amplitude 10 cm/s; (b) a tidal ellipse with period 24 hr and both clockwise and counterclockwise components; and (c) a superposition of (a) and (b) with a mean current of 10 cm/s to the ENE.

Determining velocity from position is the inverse of the illustration above. The problem may be stated as: from position estimates at irregularly spaced times, estimate the six coefficients that give the best fit of (2) to the observations, in a least-squares sense, over some time interval comparable to the period of the lowest frequency oscillation. The technique is a generalization of one introduced by Perkins (1970) in the analysis of inertial waves in current meter records and used by McPhee (1980) in analyzing AIDJEX ice drift. In essence, it is closely related to estimating spectral density at discrete frequencies over a limited time peri-

od, and was called "complex demodulation" by Perkins. Naturally, the technique works best if there are strong signals at the chosen frequencies.

Using standard least-squares techniques applied to complex numbers, the problem reduces to solving a system of linear equations.

With the following notation:

$$B(\alpha) = (i/\alpha)(e^{-i\alpha} - 1)$$

$$\Sigma = \sum_{i=1}^{N}$$

where N is the number of position samples in the fitting period, the equation in matrix form is

$$\begin{bmatrix} N & \Sigma t & \Sigma B(f) & \Sigma B(-f) & \Sigma B(\omega) & \Sigma B(-\omega) & X_0 & \Sigma X \\ \cdot & \cdot & \cdot & \cdot & \cdot & \cdot & \cdot & \cdot \\ \cdot & \Sigma t^2 & \Sigma t B(f) & \cdots\cdots\cdots & & \Sigma t B(-\omega) & V_m & \Sigma t X \\ \cdot & \cdot & \cdot & \cdot & \cdot & \cdot & \cdot & \cdot \\ \cdot & \cdot & \Sigma B(f)B(f) & \cdots\cdots\cdots & & \Sigma B(f)B(-\omega) & S_{cw} = & \Sigma B(f)X \\ \cdot & \cdot & \cdot & \cdot & \cdot & \cdot & \cdot & \cdot \\ \cdot & \cdot & \cdot & \cdot & \cdot & \cdot & S_{ccw} & \cdot \\ \cdot & \cdot & \cdot & \cdot & \cdot & \cdot & \cdot & \cdot \\ \cdot & \cdot & \cdot & \cdot & \cdot & \cdot & D_{cw} & \cdot \\ \cdot & \cdot & \cdot & \cdot & \cdot & \cdot & \cdot & \cdot \\ \cdot & \cdot & \cdot & \cdot & \cdot & \Sigma B(-\omega)B(-\omega) & D_{ccw} & \Sigma B(-\omega)X \end{bmatrix}$$

and is solved by Gaussian elimination.

Figure 2 shows the trajectory of the M/V *Polarbjørn* during the drift-station phase as it was plotted on the ship. Only fixes that were obviously erroneous were omitted. The striking diurnal loops were unexpected, and suggest a considerable tidal forcing, since the inertial period at 81 °N is about 12.2 hr.

Position and velocity are represented in a cartesian co-ordinate system consisting of a plane centered at the pole with x increasing along a line projected from the 90 °W meridian and y increasing along a projection of the Greenwich Meridian. Since the station drift was centered near 7 °E longitude, positive velocity components u and v represent approximately eastward and northward motion respectively. The transformation from geographic co-ordinates is

$$X = (x + iy) = R^*(\sin\lambda + i\cos\lambda)$$

where R = (90-lat)*111.2 km and λ is the longitude, east positive.

The fitting procedure described in the previous section was applied to the data shown in Figure 2 in two passes. First, a fit for four of the components (X_0, V_m, S_{cw}, and S_{ccw}) was calculated every 3 hr from day 179.5 to 189.5 using available fixes from the preceding and succeeding 6 hr (12-hr data window). This fit passed nearly all of the 24-hr energy and showed a smaller total least-squared error than a similar four-component fit for the diurnal coefficients. The original SATNAV fixes were then compared with the positions as calculated by the fit, and removed from the data time series whenever they deviated by more than 500 m from

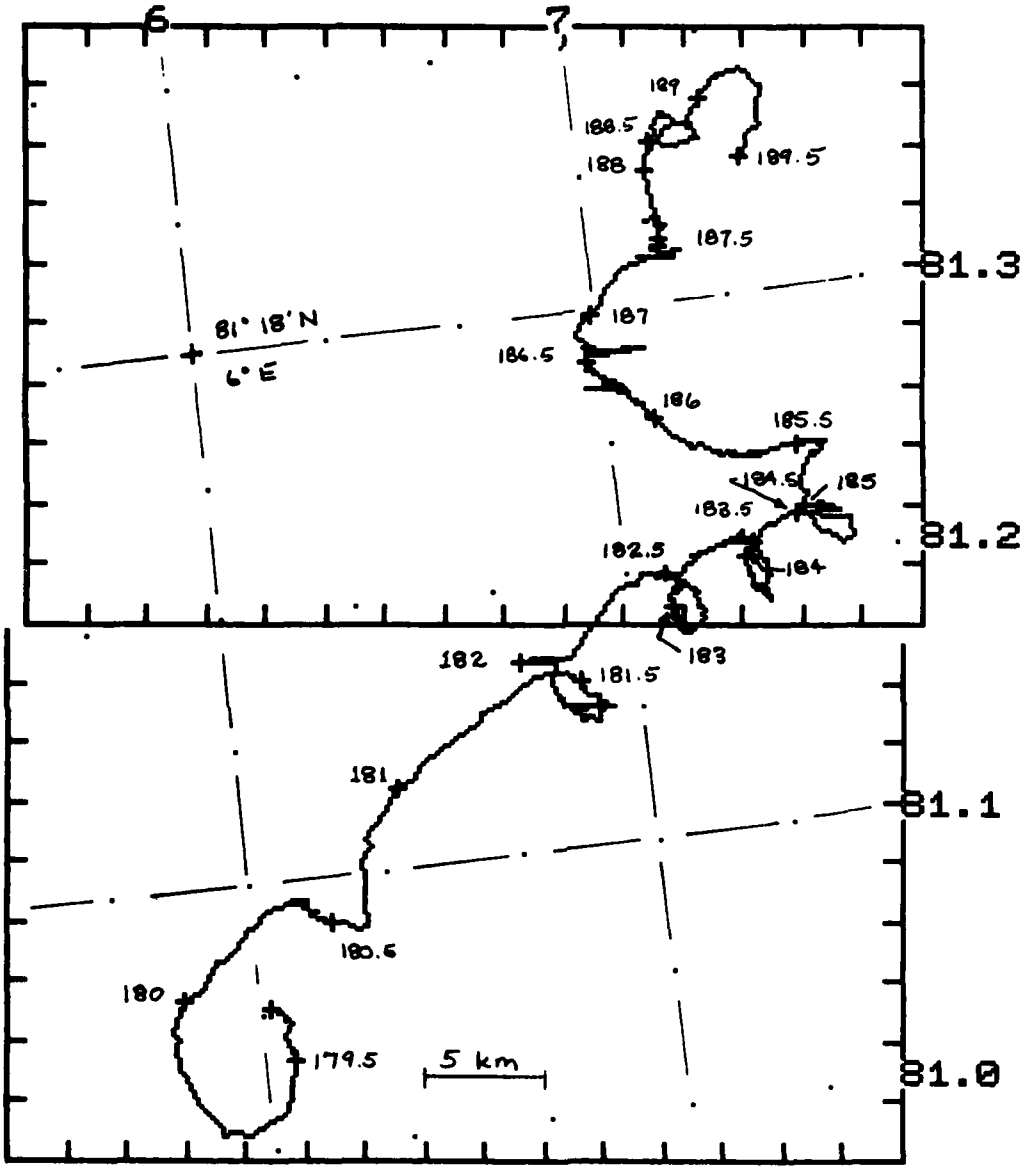

Fig. 2. Plot of SATNAV positions as received at the Polarbjørn *during the drift-station phase of the MIZEX 83 experiment.*

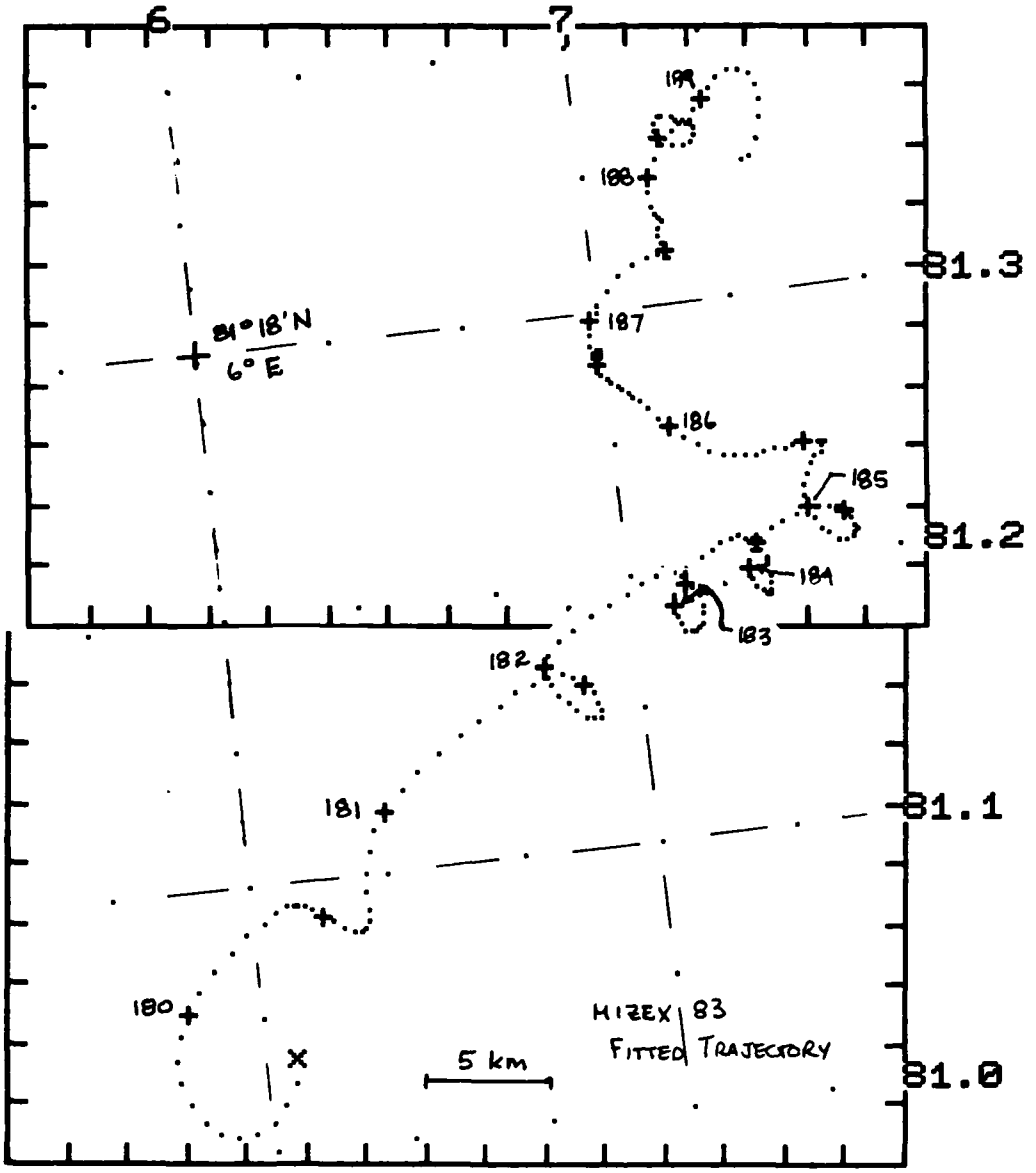

Fig. 3. Fitted trajectory of the drift station. Each dot represents 1 hr, with pluses at half-daily intervals.

the fit. On the second pass, the data (minus the out-of-bounds points) were fitted to the full 6 (complex)-component expression using the inertial period (12.2 hr) for the semidiurnal components and 24 hr for the diurnal. After some experimentation, the data window for each fit calculation was also set at 24 hr. Fit coefficients were calculated every 3 hr. All the calculations were performed on an Apple II microcomputer.

Figure 3 shows the fitted trajectory with time marks. Figure 4 shows a direct comparison of the fitted curves with all observations used in the fits. Figure 5 shows (a) the total velocity component, where the heavy line represents the real part, u, and the light line the imaginary, v; (b) the "mean" velocity; (c) the semidiurnal part, consisting of

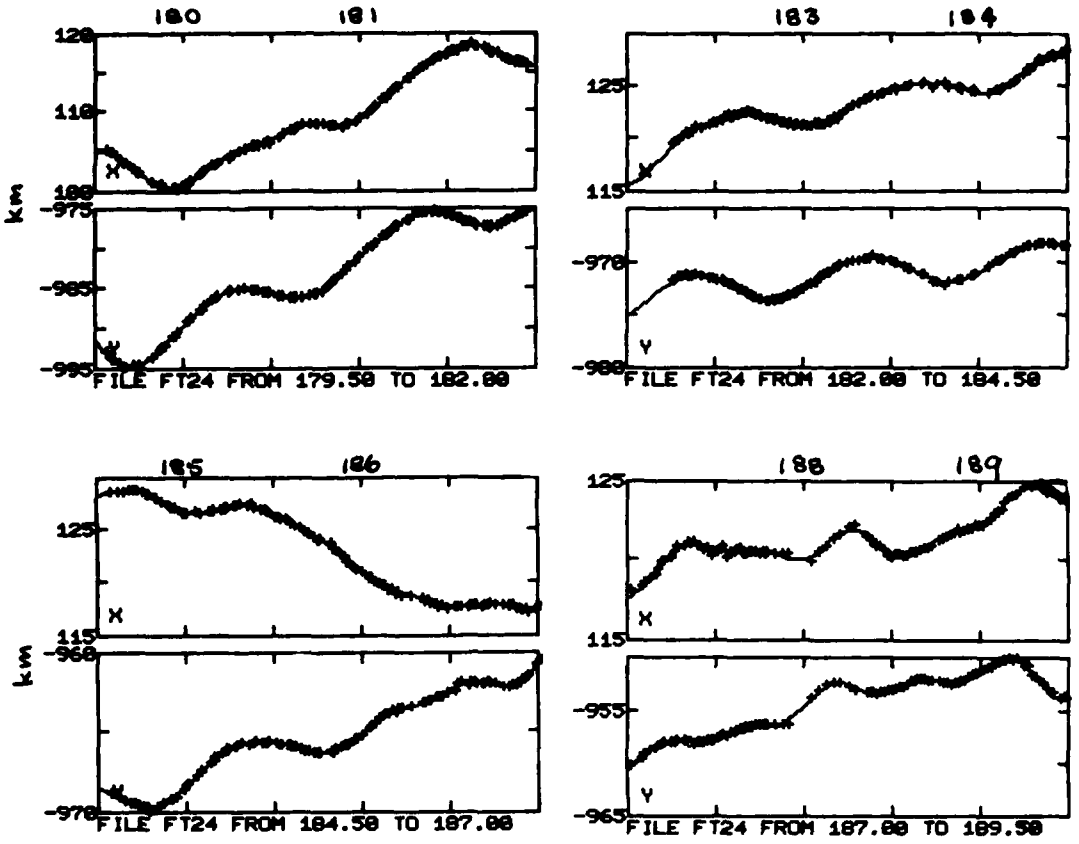

Fig. 4. Comparison of fitted positions with observations used in calculating the fixes.

$$V_f = S_{cw} \exp(-ift) + S_{ccw} \exp(ift);$$

and (d) the diurnal part,

$$V_t = D_{cw} \exp(-i\omega t) + D_{ccw} \exp(i\omega t).$$

While the emphasis in this note is not on interpretation, the semidiurnal component has been labeled "inertial," while the diurnal is called "tidal." One is hard pressed to explain the 24-hr cycle in terms other than tides, and the lunar phase (full on 25 June, day 176; last quarter on 3 July, day 184) is consistent with the attenuation of the diurnal signal seen in the first half of the record. The semidiurnal part could also be tidal, but seems to coincide with what small wind forcing there was (evidenced also in the mean velocity), prompting the label "inertial." Clearly, that identification remains tentative.

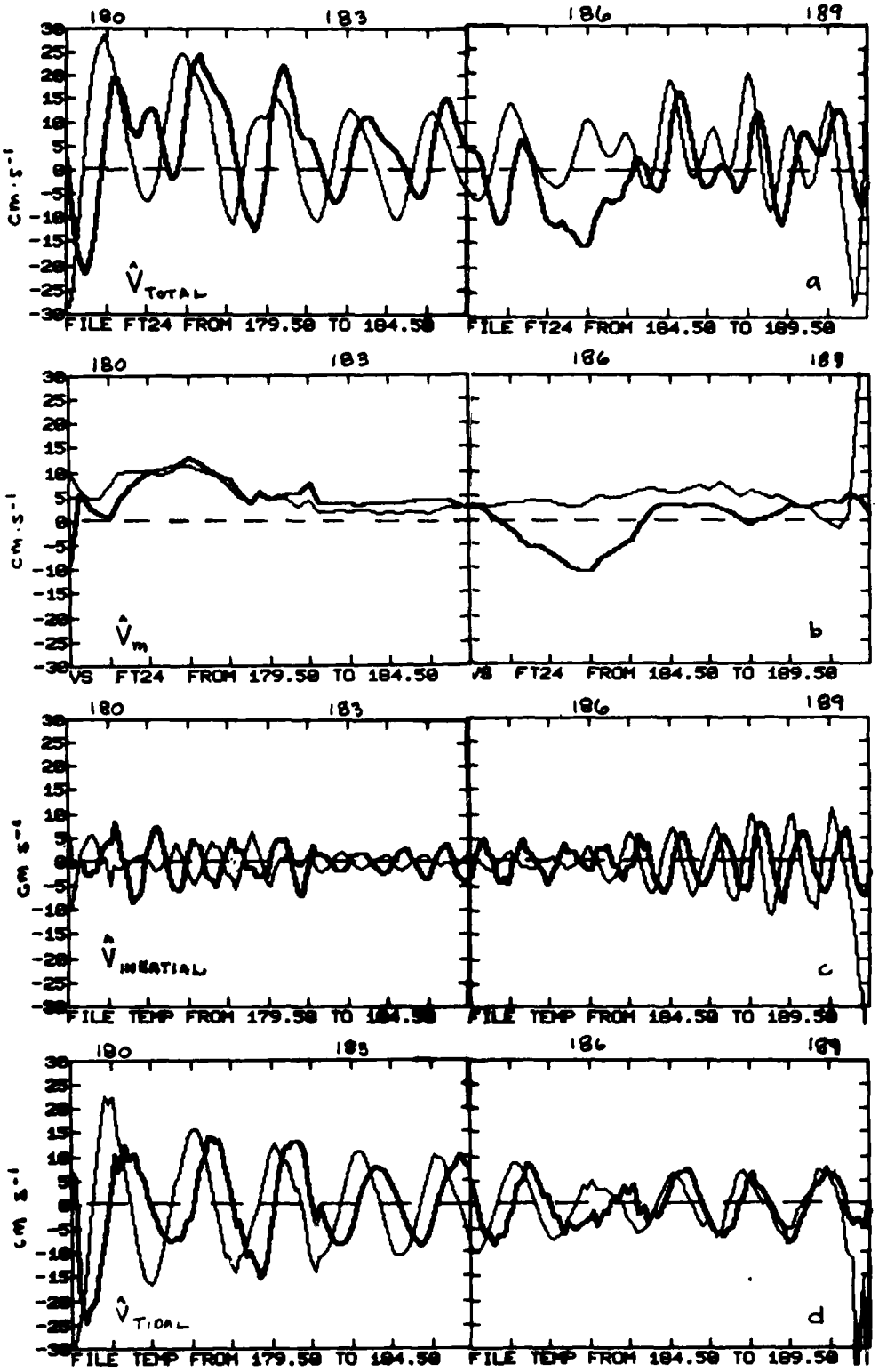

Fig. 5. (a) Total velocity, u *(real)-dark;* v *(imaginary)-light;* u *and* v *are approximately eastward and northward respectively; (b) mean velocity, V_m; (c) semidiurnal velocity (12.2-hr period); and (d) diurnal velocity.*

REFERENCES

McPhee, M.G., A study of oceanic boundary-layer processes including inertial oscillation at three drifting stations in the Arctic Ocean, *J. Phys. Oceanogr., 10,* 870–884, 1980.

Perkins, H., Inertial oscillations in the Mediterranean. Ph.D. thesis, 155 pp., Mass. Inst. of Tech., Woods Hole, Mass., 1970.

APPENDIX

Following is a listing of hourly values of position (X) in km and velocity (V) in cm/s in the coordinate system described in the text. The first component of velocity is approximately eastward positive; the second is approximately northward.

	$\hat{X}$	$\hat{V}$		$\hat{X}$	$\hat{V}$
Day 179:					
			12	(105.38,-991.46)	(2.51,-28.65)
13	(105.34,-992.51)	(-4.95,-28.57)	14	(104.93,-993.43)	(-12.24,-23.67)
15	(014.30,-994.17)	(-16.64,-16.73)	16	(103.75,-994.61)	(-19.42, -7.91)
17	(103.03,-994.73)	(-21.44, 0.65)	18	(102.27,-994.55)	(-20.69, 9.24)
19	(101.57,-994.08)	(-17.82, 16.50)	20	(100.96,-993.39)	(-13.73, 21.94)
21	(100.58,-992.53)	(-7.30, 25.29)	22	(100.44,-991.59)	(-0.37, 26.76)
23	(100.55,-990.59)	(5.84, 28.57)	24	(100.86,-989.59)	(11.22, 26.96)
Day 180:					
1	(101.34,-988.66)	(16.06, 24.44)	2	(101.94,-987.81)	(19.90, 23.96)
3	(102.66,-987.01)	(19.71, 20.62)	4	(103.34,-986.33)	(17.46, 16.78)
5	(103.97,-985.79)	(16.36, 13.15)	6	(104.49,-985.39)	(12.33, 9.03)
7	(104.86,-985.14)	(8.82, 5.08)	8	(105.17,-985.03)	(7.97, 1.73)
9	(105.44,-985.02)	(7.20, -1.31)	10	(105.71,-985.11)	(7.90, -3.77)
11	(106.05,-985.28)	(11.02, -5.69)	12	(106.48,-985.50)	(12.47, -6.52)
13	(106.94,-985.73)	(13.00, -6.23)	14	(107.37,-985.94)	(12.70, -5.11)
15	(107.80,-986.08)	(10.63, -2.34)	16	(108.12,-986.10)	(7.29, 1.55)
17	(108.31,-985.94)	(3.75, 6.39)	18	(108.38,-985.63)	(0.37, 11.06)
19	(108.35,-985.15)	(-1.75, 15.53)	20	(108.30,-984.50)	(-1.31, 20.68)
21	(108.27,-983.71)	(0.41, 23.34)	22	(108.35,-982.84)	(4.04, 24.63)
23	(108.61,-981.95)	(10.02, 24.64)	24	(109.06,-981.07)	(15.20, 23.98)
Day 181:					
1	(109.69,-980.23)	(19.70, 22.93)	2	(110.44,-979.43)	(22.17, 21.36)
3	(111.27,-978.68)	(24.15, 20.34)	4	(112.16,-977.96)	(24.65, 19.35)
5	(113.01,-977.30)	(22.12, 17.32)	6	(113.78,-976.71)	(20.86, 15.69)
7	(114.51,-976.18)	(19.55, 13.29)	8	(115.18,-975.76)	(17.25, 8.93)
9	(115.78,-975.51)	(16.36, 4.70)	10	(116.36,-975.42)	(15.61, 0.17)
11	(116.90,-975.50)	(13.89, -5.23)	12	(117.37,-975.76)	(12.13, -8.55)
13	(117.76,-976.10)	(9.40,-10.28)	14	(117.96,-976.52)	(4.35,-11.29)
15	(118.05,-976.88)	(0.79, -8.79)	16	(118.02,-977.13)	(-2.92, -4.72)
17	(117.80,-977.24)	(-7.66, -0.51)	18	(117.48,-977.17)	(-9.98, 4.42)
19	(117.10,-976.93)	(-11.09, 8.45)	20	(116.70,-976.59)	(-12.75, 9.54)
21	(116.26,-976.22)	(-11.31, 10.81)	22	(115.91,-975.82)	(-8.05, 11.27)
23	(115.64,-975.45)	(-3.84, 10.85)	24	(115.61,-975.05)	(2.52, 11.28)
Day 182:					
1	(115.82,-974.63)	(9.12, 12.17)	2	(116.31,-974.06)	(14.65, 14.15)
3	(116.92,-973.54)	(18.65, 14.82)	4	(117.64,-973.00)	(20.77, 14.98)
5	(118.33,-972.48)	(22.54, 13.34)	6	(119.11,-972.01)	(20.88, 12.18)
7	(119.81,-971.61)	(17.76, 10.12)	8	(120.40,-971.27)	(14.34, 5.54)
9	(120.84,-971.14)	(10.58, 1.76)	10	(121.17,-971.15)	(7.74, -1.84)
11	(121.35,-971.31)	(6.80, -4.72)	12	(121.60,-971.52)	(6.69, -6.82)
13	(121.84,-971.80)	(6.65, -8.41)	14	(122.12,-972.09)	(4.91,-10.03)
15	(122.26,-972.47)	(2.92,-10.66)	16	(122.33,-972.85)	(0.63,-10.15)
17	(122.31,-973.18)	(-1.71, -8.26)	18	(122.20,-973.43)	(-3.87, -5.61)
19	(122.03,-973.57)	(-5.54, -2.27)	20	(121.81,-973.60)	(-6.61, 1.55)
21	(121.57,-973.48)	(-6.49, 5.25)	22	(121.36,-973.23)	(-5.31, 8.40)
23	(121.19,-972.89)	(-3.19, 10.54)	24	(121.13,-972.48)	(-0.32, 11.99)

	$\hat{X}$	$\hat{V}$		$\hat{X}$	$\hat{V}$
Day 183:					
1	(121.17,-972.04)	(2.79, 12.58)	2	(121.32,-971.59)	(5.45, 12.51)
3	(121.56,-971.15)	(7.95, 11.79)	4	(121.89,-970.74)	(9.80, 10.61)
5	(122.26,-970.39)	(11.03, 9.28)	6	(122.66,-970.09)	(11.33, 7.58)
7	(123.06,-969.85)	(10.93, 5.64)	8	(123.46,-969.69)	(10.02, 3.15)
9	(123.80,-969.62)	(8.74, 0.94)	10	(124.09,-969.62)	(7.49, -1.34)
11	(124.34,-969.70)	(6.39, -3.69)	12	(124.55,-969.88)	(5.52, -6.01)
13	(124.74,-970.13)	(4.80, -8.04)	14	(124.90,-970.46)	(4.26, -9.80)
15	(125.03,-970.83)	(3.39,-10.35)	16	(125.13,-971.19)	(2.14, -9.83)
17	(125.19,-971.52)	(0.69, -8.13)	18	(125.18,-971.77)	(-1.29, -5.60)
19	(125.10,-971.92)	(-3.28, -2.45)	20	(124.96,-971.95)	(-4.56, 0.85)
21	(124.78,-971.85)	(-5.58, 4.24)	22	(124.57,-971.64)	(-5.57, 7.27)
23	(124.38,-971.34)	(-4.38, 9.74)	24	(124.27,-970.96)	(-1.73, 11.37)
Day 184:					
1	(124.27,-970.53)	(1.88, 12.13)	2	(124.41,-970.10)	(5.75, 12.39)
3	(124.69,-969.67)	(9.53, 11.63)	4	(125.09,-969.27)	(12.54, 10.26)
5	(125.58,-968.94)	(14.65, 9.09)	6	(126.12,-968.65)	(15.01, 7.06)
7	(126.65,-968.43)	(14.00, 4.77)	8	(127.09,-968.31)	(11.38, 2.40)
9	(127.46,-968.26)	(9.34, 0.28)	10	(127.77,-968.29)	(7.49, -1.60)
11	(127.99,-968.37)	(5.33, -2.76)	12	(128.17,-968.49)	(4.52, -4.04)
13	(128.33,-968.66)	(4.16, -5.08)	14	(128.47,-968.86)	(3.86, -5.87)
15	(128.60,-969.08)	(3.01, -6.07)	16	(128.68,-969.29)	(1.36, -5.65)
17	(128.67,-969.47)	(-2.46, -4.71)	18	(128.53,-969.60)	(-5.06, -2.91)
19	(128.31,-969.67)	(-7.43, -0.40)	20	(128.00,-969.62)	(-10.45, 2.71)
21	(127.61,-969.47)	(-11.03, 5.88)	22	(127.22,-969.20)	(-10.10, 8.84)
23	(126.90,-968.84)	(-9.13, 11.54)	24	(126.63,-968.40)	(-5.75, 13.12)
Day 185:					
1	(126.49,-967.91)	(-1.72, 13.65)	2	(126.48,-967.43)	(1.03, 13.32)
3	(126.59,-966.97)	(4.26, 12.04)	4	(126.78,-966.57)	(6.27, 10.16)
5	(127.00,-966.25)	(5.17, 8.27)	6	(127.18,-965.99)	(4.29, 6.18)
7	(127.30,-965.80)	(2.42, 4.23)	8	(127.36,-965.68)	(-0.20, 2.54)
9	(127.29,-965.61)	(-3.23, 1.10)	10	(127.13,-965.59)	(-6.13, -0.07)
11	(126.82,-965.61)	(-9.44, -1.32)	12	(126.46,-965.67)	(-10.57, -2.09)
13	(126.07,-965.76)	(-10.79, -2.62)	14	(125.68,-965.85)	(-11.55, -3.34)
15	(125.28,-965.97)	(-10.90, -3.41)	16	(124.89,-966.09)	(-10.37, -2.99)
17	(124.50,-966.18)	(-11.88, -2.35)	18	(124.06,-966.24)	(-12.25, -0.86)
19	(123.61,-966.24)	(-12.90, 1.14)	20	(123.14,-966.16)	(-14.23, 3.41)
21	(122.61,-965.99)	(-15.06, 5.76)	22	(122.06,-965.75)	(-15.52, 7.82)
23	(121.50,-965.42)	(-15.41, 10.09)	24	(120.95,-965.04)	(-14.66, 10.62)
Day 186:					
1	(120.45,-964.67)	(-13.28, 10.16)	2	(120.00,-964.31)	(-10.06, 9.54)
3	(119.67,-964.00)	(-8.43, 7.67)	4	(119.39,-963.76)	(-7.36, 5.67)
5	(119.17,-963.57)	(-5.77, 4.09)	6	(118.96,-963.45)	(-6.07, 3.10)
7	(118.73,-963.34)	(-6.68, 3.01)	8	(118.49,-963.22)	(-5.94, 3.45)
9	(118.27,-963.07)	(-6.11, 4.68)	10	(118.05,-962.88)	(-5.75, 6.00)
11	(117.89,-962.64)	(-3.22, 7.75)	12	(117.80,-962.36)	(-1.93, 7.62)
13	(117.75,-962.10)	(-0.61, 6.20)	14	(117.78,-961.92)	(2.83, 4.23)
15	(117.88,-961.82)	(2.70, 1.19)	16	(117.96,-961.83)	(1.43, -1.67)
17	(118.02,-961.93)	(1.37, -3.35)	18	(118.02,-962.06)	(-1.24, -3.57)
19	(117.93,-962.16)	(-3.64, -1.89)	20	(117.80,-962.17)	(-3.9[illegible], 1.21)
21	(117.65,-962.05)	(-4.08, 5.88)	22	(117.52,-961.74)	(-2.53, 10.91)
23	(117.49,-961.28)	(0.66, 15.11)	24	(117.58,-960.68)	(4.91, 18.03)

	$\hat{X}$	$\hat{V}$		$\hat{X}$	$\hat{V}$
DAY 187					
1	(117.84,-960.01)	(9.50, 18.86)	2	(118.28,-959.35)	(13.47, 17.74)
3	(118.81,-958.77)	(15.83, 14.45)	4	(119.39,-958.32)	(16.23, 9.96)
5	(119.95,-958.04)	(14.21, 5.78)	6	(120.41,-957.91)	(10.99, 1.72)
7	(120.73,-957.90)	(6.92, -0.92)	8	(120.90,-957.96)	(3.17, -1.42)
9	(120.95,-958.00)	(-0.17, -0.40)	10	(120.90,-957.98)	(-2.42, 1.82)
11	(120.80,-957.88)	(-3.40, 3.99)	12	(120.68,-957.69)	(-3.32, 6.58)
13	(120.58,-957.42)	(-2.37, 8.24)	14	(120.48,-957.08)	(-0.75, 8.74)
15	(120.49,-956.79)	(0.73, 7.10)	16	(120.53,-956.58)	(1.43, 4.48)
17	(120.57,-956.51)	(0.68, 1.44)	18	(120.58,-956.48)	(-0.41, 0.28)
19	(120.54,-956.46)	(-1.85, 0.87)	20	(120.38,-956.43)	(-4.29, 3.14)
21	(120.22,-956.24)	(-4.10, 7.59)	22	(120.10,-955.87)	(-2.55, 12.67)
23	(120.03,-955.32)	(-1.18, 17.63)	24	(120.05,-954.63)	(2.54, 20.08)
Day 188:					
1	(120.21,-953.91)	(6.56, 19.77)	2	(120.54,-953.27)	(10.96, 16.64)
3	(120.96,-952.76)	(12.08, 11.45)	4	(121.38,-952.46)	(10.84, 5.07)
5	(121.69,-952.39)	(8.08, -2.34)	6	(121.90,-952.57)	(3.39, -6.86)
7	(121.92,-952.85)	(-2.00, -8.59)	8	(121.77,-953.17)	(6.19, -7.19)
9	(121.48,-953.37)	(-9.78, -3.45)	10	(121.09,-953.41)	(-11.23, 1.37)
11	(120.66,-953.26)	(-9.10, 5.31)	12	(120.39,-953.01)	(-5.73, 8.31)
13	(120.26,-952.69)	(-1.53, 9.24)	14	(120.27,-952.39)	(2.15, 7.10)
15	(120.41,-952.18)	(5.56, 4.35)	16	(120.65,-952.08)	(7.61, 1.07)
17	(120.97,-952.10)	(8.07, -2.17)	18	(121.24,-952.20)	(6.96, -3.52)
19	(121.46,-952.33)	(5.19, -2.85)	20	(121.62,-952.41)	(4.24, -1.78)
21	(121.75,-952.40)	(3.23, 2.78)	22	(121.87,-952.20)	(3.31, 8.06)
23	(122.01,-951.84)	(4.80, 11.44)	24	(122.22,-951.37)	(6.95, 14.19)
Day 189:					
1	(122.52,-950.85)	(9.48, 14.20)	2	(122.89,-950.40)	(11.42, 10.32)
3	(123.33,-950.12)	(12.68, 4.70)	4	(123.79,-950.08)	(12.44, -2.39)
5	(124.26,-950.24)	(10.73, -9.18)	6	(124.57,-950.70)	(6.53,-15.99)
7	(124.72,-951.36)	(1.50,-20.30)	8	(124.68,-952.09)	(-2.97,-27.41)
9	(124.51,-953.06)	(-6.23,-24.69)	10	(124.25,-953.77)	(-7.56,-13.47)
11	(123.98,-953.99)	(-5.65, 1.84)	12	(123.83,-953.38)	(-2.35, 33.66)

MIZEX 83—BIO Buoy Data Summary*

G. SYMONDS AND I. PETERSON
Bedford Institute of Oceanography, Atlantic Oceanographic Laboratory
Dartmouth, Nova Scotia, Canada

This preliminary report contains a summary of the trajectories and velocities of the six drifting buoys deployed by the Bedford Institute of Oceanography during MIZEX 83. The buoys were tracked using the ARGOS positioning system. Dates and positions of deployment and recovery are listed in Table 1. Buoy 2404 ceased operating shortly after deployment and is not included in the following figures. Buoys 2405 and 2406 were not recovered. Buoy 2406 ceased operating on 24 July 1983, while buoy 2405 continued until 19 August 1983. Buoys 2407 and 2409 were recovered at the end of the drift phase and redeployed in the East Greenland Current during the edge phase (14–23 July 1983). Buoy 2408 was recovered by R/V *Lance* on 21 July 1983.

Also listed in Table 1 are the standard deviations in the u (eastward) and v (northward) components of velocity. In this report, velocity is computed from 1-hr linearly interpolated positions, and then smoothed with a 2-hr running mean. The relatively high standard deviation for buoy 2409 is due largely to instrument error, since, at a fixed location on land before the field experiment, the standard deviation of position for buoy 2409 was about twice that for the other buoys.

Mean trajectories were computed from 2-hr linearly interpolated positions with a 24-hr running mean. Trajectories of the three buoys deployed prior to the drift phase (2405, 2406, and 2408) are plotted in Figure 1. The trajectories of buoys 2407 and 2409 are shown both during the drift phase (Figure 2) and later during the edge phase (Figure 3).

A listing of 24-hr-averaged positions for each buoy is given in Table 2.

Table 1. Deployment and recovery dates and positions and standard deviations of velocity for the BIO buoys.

Buoy	Deployment		Recovery		Length	S.D. (cm/s)	
no.	Date	Position	Date	Position	(days)	u	v
2404	18 Jun 83	80.68°N, 12.09°E	20 Jun 83	80.51°N, 12.69°E	3	—	—
2405	18 Jun 83	81.37°N, 10.60°E	19 Aug 83	80.69°N, 5.92°E	63	09.38	7.78
2406	18 Jun 83	81.02°N, 09.08°E	24 Jul 83	80.52°N, 11.03°E	37	9.87	8.82
2407	18 Jun 83	80.60°N, 11.61°E	21 Jun 83	80.33°N, 11.76°E	4	—	—
2407	27 Jun 83	80.86°N, 08.55°E	10 Jul 83	81.03°N, 09.52°E	14	8.66	8.30
2407	14 Jul 83	79.35°N, 01.44°E	22 Jul 83	78.29°N, 03.80°E	9	—	—
2408	18 Jun 83	80.83°N, 13.00°E	21 Jul 83	80.53°N, 21.11°E	34	12.79	10.76
2409	27 Jun 83	81.06°N, 08.62°E	8 Jul 83	81.09°N, 09.80°E	12	13.47	9.89
2409	14 Jul 83	79.36°N, 01.82°E	22 Jul 83	78.57°N, 03.50°E	9	—	—

*This report is meant only as a very brief summary for interested MIZEX scientists and should not be considered a final scientific publication.

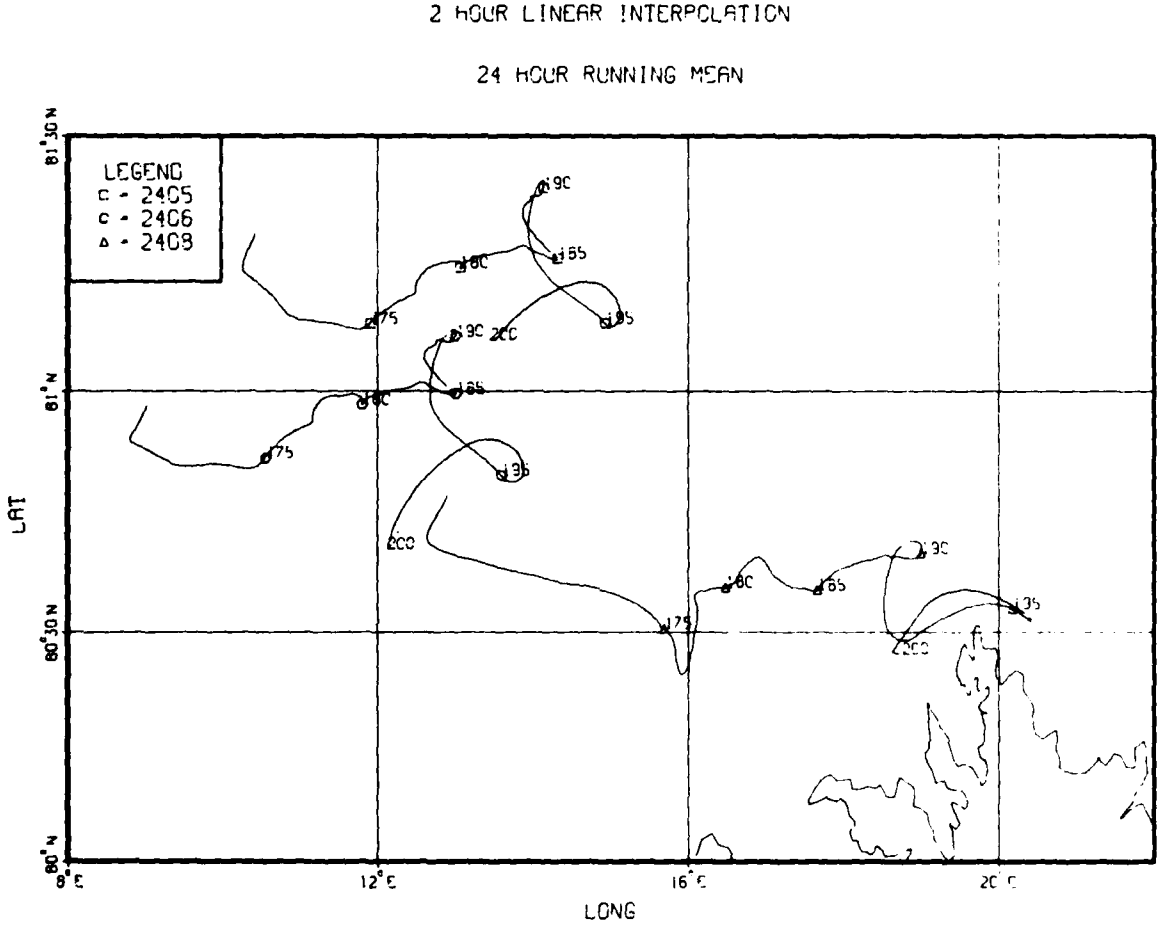

Fig. 1. Trajectories (24-hr running mean) for buoys 2405, 2406 and 2408 (19 June–19 July 1983). Julian days correspond to mean position centered at 0000 hr.

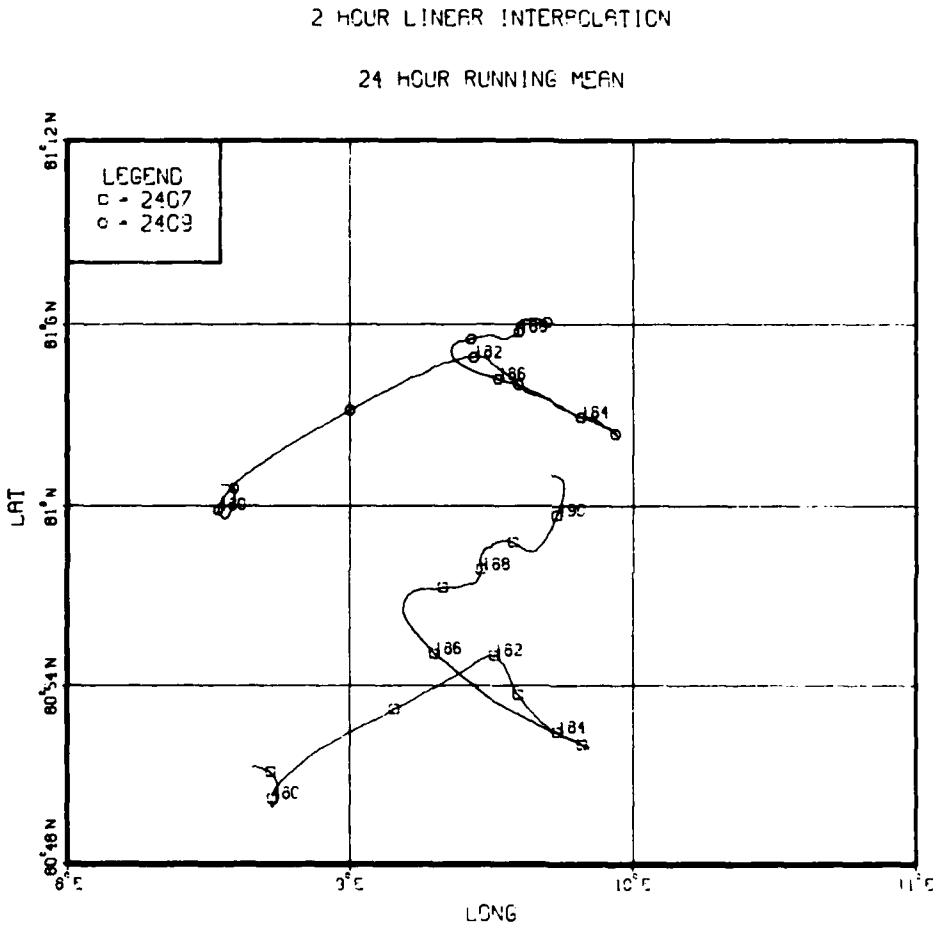

Fig. 2. Trajectories (24-hr running mean) for buoys 2407 and 2409 during drift phase.

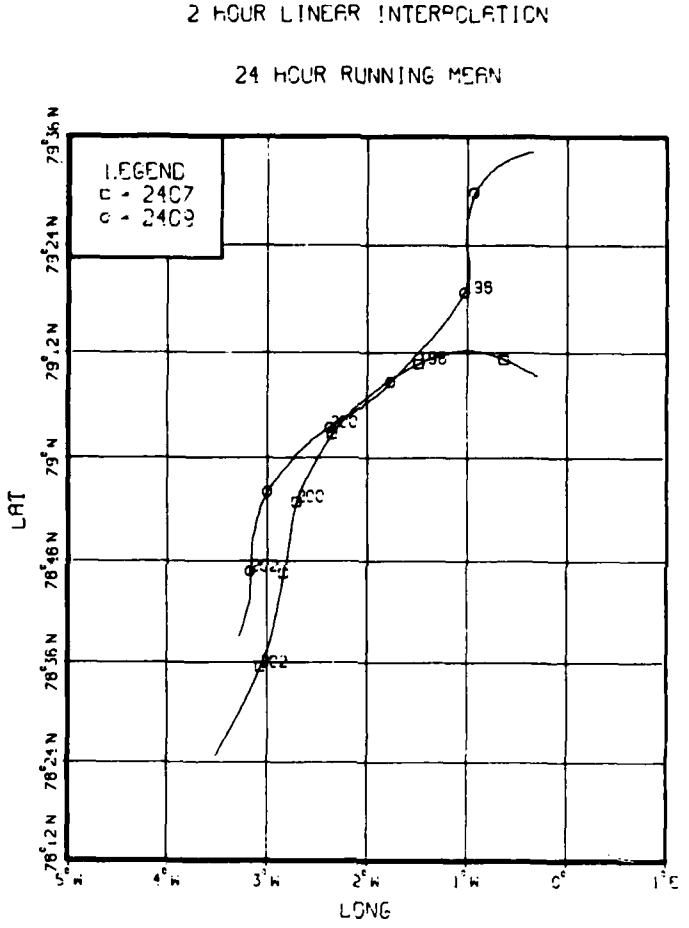

Fig. 3. Trajectories (24-hr running mean) for buoys 2407 and 2409 during edge phase.

Table 2. 24-hr averaged positions for all buoys deployed during MIZEX 83 (centered at 0000 hr).

Day	*Lat.*	*Long.*	*Day*	*Lat.*	*Long.*
Buoy 2405					
171	81.252	10.252	201	81.097	13.387
172	81.196	10.607	202	81.057	13.435
173	81.143	10.990	203	81.050	13.535
174	81.129	11.574	204	81.048	13.453
175	81.135	11.898	205	81.048	13.344
176	81.185	12.356	206	81.057	13.153
177	81.218	12.516	207	81.057	13.100
178	81.253	12.781	208	81.061	12.999
179	81.256	13.063	209	81.058	13.057
180	81.245	13.060	210	81.071	13.018
181	81.273	13.466	211	81.104	12.720
182	81.288	13.848	212	81.126	12.494
183	81.281	13.971	213	81.121	12.434
184	81.268	14.171	214	81.106	12.621
185	81.264	14.316	215	81.103	12.726
186	81.308	14.017	216	81.121	12.554
187	81.366	13.878	217	81.169	12.241
188	81.382	13.972	218	81.197	12.028
189	81.385	14.039	219	81.194	11.964
190	81.400	14.128	220	81.220	11.793
191	81.410	14.099	221	81.238	11.668
192	81.339	13.932	222	81.256	11.087
193	81.243	14.099	223	81.213	10.545
194	81.182	14.563	224	81.186	9.274
195	81.136	14.926	225	81.154	8.350
196	81.144	15.115	226	81.072	7.836
197	81.210	14.900	227	81.028	6.968
198	81.187	14.108	228	80.977	6.527
199	81.111	13.549	229	80.932	6.216
200	81.104	13.434	230	80.865	5.925
			231	80.766	5.829
Buoy 2406					
171	80.907	8.798	188	81.101	12.766
172	80.870	9.157	189	81.101	12.869
173	80.848	9.627	190	81.110	12.997
174	80.845	10.192	191	81.118	12.917
175	80.864	10.551	192	81.039	12.683
176	80.927	11.028	193	80.945	12.778
177	80.959	11.182	194	80.887	13.175
178	80.991	11.445	195	80.829	13.593
179	80.990	11.771	196	80.824	13.856
180	80.974	11.801	197	80.893	13.647
181	81.002	12.198	198	80.862	12.864
182	81.017	12.541	199	80.745	12.261
183	81.011	12.659	200	80.676	12.112
184	80.998	12.849	201	80.620	11.995
185	80.995	13.006	202	80.600	11.666
186	81.040	12.700	203	80.604	11.229
187	81.087	12.658	204	80.528	10.716

Day	*Lat.*	*Long.*	*Day*	*Lat.*	*Long.*
Buoy 2407					
179	80.852	8.718	188	80.965	9.463
180	80.837	8.722	189	80.980	9.576
181	80.887	9.156	190	80.995	9.731
182	80.917	9.510	197	79.187	-0.637
183	80.895	9.595	198	79.179	-1.502
184	80.874	9.732	199	79.045	-2.362
185	80.867	9.818	200	78.915	-2.718
186	80.918	9.295	201	78.776	-2.843
187	80.955	9.328	202	78.591	-3.079
Buoy 2408					
171	80.706	12.627	187	80.646	18.148
172	80.653	13.209	188	80.659	18.461
173	80.610	14.253	189	80.659	18.743
174	80.574	15.166	190	80.667	18.994
175	80.509	15.677	191	80.693	18.861
176	80.461	15.834	192	80.609	18.536
177	80.416	15.957	193	80.488	18.668
178	80.542	16.120	194	80.519	19.165
179	80.588	16.170	195	80.551	20.172
180	80.596	16.484	196	80.523	20.424
181	80.638	16.716	197	80.576	19.936
182	80.660	16.903	198	80.463	19.051
183	80.6[illegible]	17.024	199	80.558	18.628
184	80.595	17.370	200	80.454	18.736
185	80.590	17.668	201	80.493	19.421
186	80.611	17.783	202	80.525	20.556
Buoy 2409					
179	81.010	8.587	188	81.096	9.595
180	80.998	8.532	189	81.101	9.695
181	81.053	9.000			
182	81.082	9.437	197	79.497	-0.936
183	81.067	9.593	198	79.313	-1.042
184	81.049	9.815	199	79.144	-1.779
185	81.040	9.937	200	79.058	-2.383
186	81.070	9.520	201	78.934	-3.009
187	81.092	9.425	202	78.780	-3.176

MIZEX 83 Mesoscale Sea Ice Dynamics: Initial Analysis

W.D. HIBLER III
U.S. Army Cold Regions Research and Engineering Laboratory
Hanover, New Hampshire 03755-1290

M. LEPPARANTA
Institute of Marine Research
Helsinki, Finland

This report describes the basic characteristics of the mesoscale sea ice dynamics data set taken during the drifting phase of the MIZEX 83 pilot study. The basic data set consists of distance measurements accurate to 1-2 m between Del Norte units at five sites with one site being the ship. In addition to these measurements, the overall rotation of the array was determined with less accuracy by using the ship's radar to measure the angles of either active or passive radar transponders on the ice at 2-hr intervals.

The basic configuration of the array is shown in Figure 1, which is drawn to scale for 29 June 0800 GMT. Each complete Del Norte measurement consists of measuring directly the 7 distances d_0, d_1, d_2, d_3, b_1, b_2, b_3 as noted in this figure. These distances are measured to an acccuracy of 1-2 m. Other distances are triangulated and will be less accurate, with the precise measurement error depending on the geometry of the array. It was initially planned to make measurements every hour or so, but once data began to be acquired it became obvious that shorter time intervals would be necessary to resolve all motion occurring. Accordingly, the acquisition computer was reprogrammed to automatically acquire data at 3-min intervals. This operational mode was employed throughout the experiment although there were occasional data gaps due to battery failure, polar bears, and interference from less accurate Motorola transponders located on certain floes. Such active "ship's radar" transponders will not be necessary in the future, as it was found that passive transponders could be effectively located for angular measurements provided their distances from the Del Norte units were known. It should also be noted that the rotation of the array is critical only when one wants the north and east components of relative ice drift. The Del Norte system itself gives the strain rate invariants very accurately without the need for any other angular measurements.

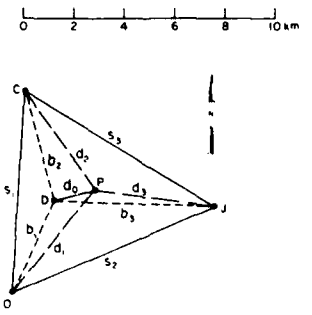

Fig. 1. Configuration of strain array and nomenclature for distances discussed later in the paper. The triangle is plotted to scale for 29 June 0800 GMT; the ship (M/V Polarbjørn*) is located at the center point P moored to an ice floe. Del Norte units are located at circled points. Directly measured distances (accurate to 1-2 m) are denoted by subscripted b's and d's while distances calculated by triangulation (less accurate depending on geometry) are denoted by subscripted* s*'s.*

While the main measurement program occurred with the ship moored to a floe, data were also taken before and after the center floe deployment with the ship moving. This was made possible by the automated nature of the system, which allowed a measurement to be made in about 15 seconds, during which time the ship's motion was relatively small. Triangulation could then be made of the relative positions of points on the ice.

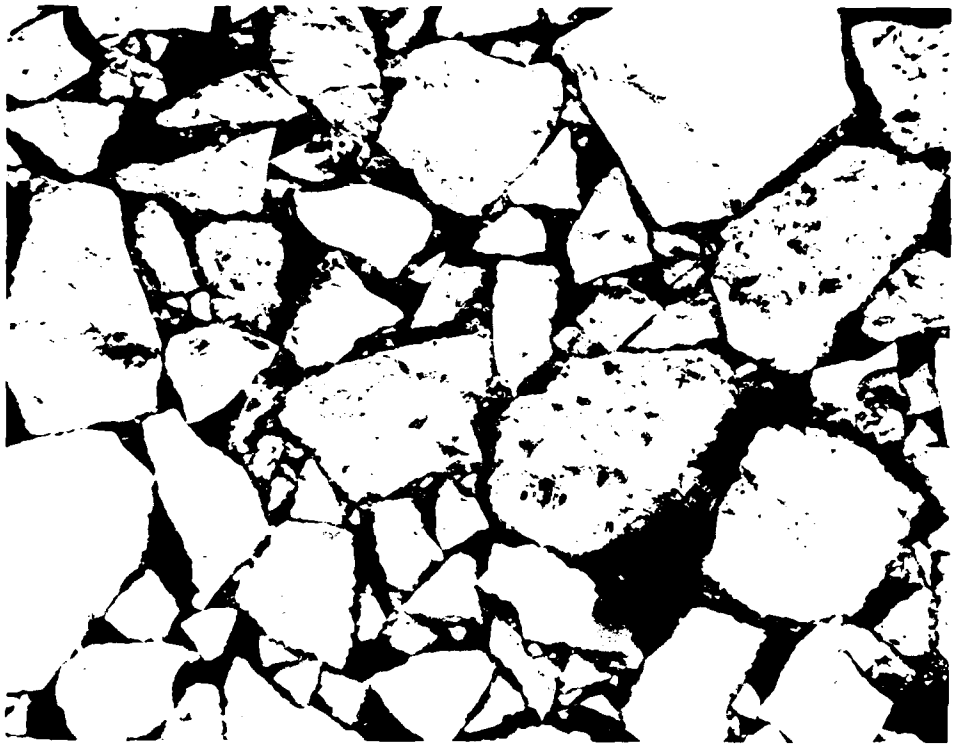

Fig. 2. Photograph of ice floes near the center of the strain array. The location of the Polarbjørn *is noted, which, for scale, is 50 m long. Photograph taken by Dr. Vernon Squires of the Scott Polar Research Institute as part of an aerial survey carried out by helicopter flights.*

In terms of the overall field operation, there were no major problems, and generally the system operated much better than expected. Battery lifetimes were about 4 days, but varied with different types of transponders. The connection system for the batteries will be improved for MIZEX 84 to facilitate battery replacement. One minor problem was that the tripod height (about 4 m) was a bit low for the initial baseline unit, which was initially at site C. To correct this, the baseline tripod was raised about 1.5 m and moved to site D. After about 5 days one master unit began malfunctioning and had to be replaced, but overall the automated nature of the system together with its high accuracy proved most valuable. These features allowed the acquisition of by far the most detailed and temporally dense ice deformation measurements in existence to date.

In addition to transponders, sites O, C and J were equipped with current meter strings moored to toroid buoys. As discussed below, the large deformation rates observed demonstrate the necessity of accurate ice deformation measurements in order to precisely interpret the current measurements. Basically, relative ice drift rates of 2 to 3 cm/s, and sometimes 8 cm/s, were common. Often these events would last for only a few hours, so fine temporal resolution becomes critical. Because of these large ice motion fluctuations, observed variations in current meter readings may in many cases be due to ice motion.

The ice pack was relatively homogeneous over the region covered by the triangle. Ice floes were typically 30–50 m in diameter, and the compactness of the ice was 80 to 90%. Figure 2 shows a photograph over the ice taken from the helicopter

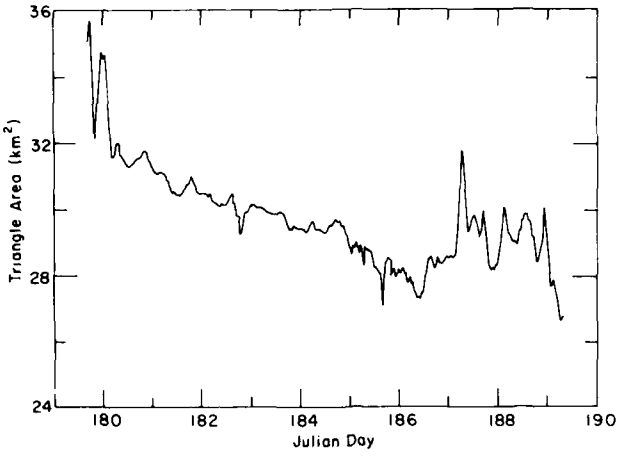

Fig. 3. The area of the triangle OCJ at ½-hr intervals filtered with a low-pass filter with transition band from 48- to 60-minute periods. The high-frequency variations during days 184.5 to 186.5 are due to problems with the measurement system (a poorly functioning master unit).

at an altitude of about 5000 ft. To a first approximation the ice pack is an almost ideal two-dimensional granular medium, and our measurement scale is good for studying its small-scale deformation. The pack was a mixture of first-year and multiyear ice, with thickness ranging from 1 to 4 m.

The overall long-term character of the deformation is shown in Figures 3 through 5. Figure 3 shows the area of the triangle at ½-hr intervals over the drift station experiment. The curve has been smoothed with a low-pass symmetric filter with 241 weights and a transition band from 48- to 60-min periods. The filter design is described in Hibler (1972). Figure 4 shows the triangle configuration at approximately the beginning, middle, and end. Further, Figure 4 shows the approximate relative position and orientation of the ice edge. As can be seen from Figure 3, the area shows a rapid opening and closing early in the experiment followed by a gradual convergence and then a major closing-opening-closing cycle during the last several days of the experiment. Examination of Figure 4 shows that this event over the last several days is accompanied by a major shearing of the triangle, with the southern points moving northeastward relative to the northern point. This overall convergence is consistent with the light southerly winds during the experiment and the generally northeastward drift, which would tend to push the ice edge back into the main pack. Note, however, that there are fluctuations on top of this trend.

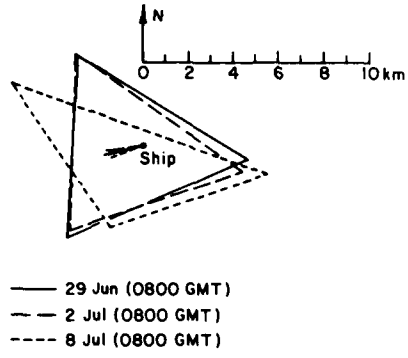

Fig. 4. Configuration change of the triangle over the period of the experiment. Also shown is the approximate location and orientation of the ice edge drawn to scale.

Moreover, although not shown there is some indication that the shearing is greater than the convergence, as one would expect for a relatively incompressible two-dimensional interacting ice field.

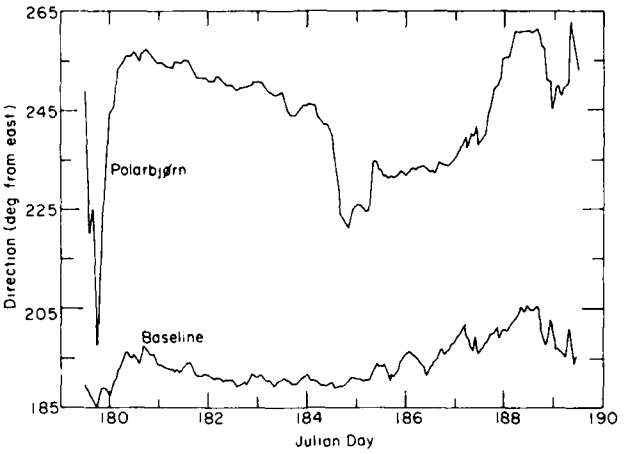

Fig. 5. Orientation of the baseline (line from the ship to site D) and the heading of M/V Polarbjørn *at 1-hr intervals over the period of the experiment. The angle increases counterclockwise, and the zero points east.*

With regard to orientation, the baseline (M/V *Polarbjørn*—site D) rotated about 20° during the drifting phase (Fig. 5). This caused a relative motion in the array comparable to the strain motion measured with the Del Norte system. Because the accuracy of the orientation angle is only 0.5°, large uncertainties arise when transforming the Del Norte data to a north-east coordinate system. These uncertainties do not, however, affect the strain rate invariants. At the distance of 5 km, a 0.5° sector is 40 m wide. Also shown in Figure 5 is the rotation of the *Polarbjørn* measured with a gyrocompass. The large bump in day 184 is man-caused because of the necessity to change the ship's mooring. The two rotation curves show similar behavior, but the high-frequency fluctuations are much more pronounced for *Polarbjørn*.

Table 1 gives the position of the Del Norte sites in north-east coordinates at 6-hr intervals. Their accuracies are $\delta x \cong 0.01 \cdot |y|$, $\delta y \cong 0.01 \cdot |x|$. These large errors are due to the orientation uncertainty discussed above. The baseline orientation is given in Table 2. Note that the direction is counted counterclockwise from the east; the numbers thus tell that the direction is slightly southward from west (see also Fig. 1). The data in Table 1 were used to estimate the zeroth and first-order terms of 6-hour mean ice velocities using the linear model (see e.g. Hibler et al., 1974)

$$u = u_0 + x \cdot \partial_x u|_0 + y \cdot \partial_y u|_0 + e_u,$$

$$v = v_0 + x \cdot \partial_x v|_0 + y \cdot \partial_y v|_0 + e_v,$$

where the subscript 0 refers to *Polarbjørn* and (e_u, e_v) is the error term. The results are presented in Table 3. The inaccuracy due to measurement error is 0.1 cm/s for the constant terms u_0 and v_0 and 0.1% h^{-1} for the first-order derivatives. Also shown are the principal strain rates (E1 and E2), the direction of the first principal axis (AE1), divergence (EI), twice the maximum shear rate (EII), and vorticity (VOR). The goodness of fit, defined as the ratio of the explained variance to the total variance (last column), is typically 85–95%.

Analysis of finer time-scale data shows that a large variety of significant fluctuations is superimposed on the overall trends. This is illustrated in Figures 6 and 7, which show raw and filtered distances at 3-min intervals. As can be seen, the filtered record shows large variations on time scales of a few hours. In the raw data, there are significant fluctuations over ½-hr intervals. These fluctuations are undoubtedly related to floe bumping as well as randomness in the forcing fields. However, it is also possible that they are due to more organized floe interactions, which can manifest themselves as kinematic waves propagating across the array. Numerical studies by Hibler et al. (1983) have shown that such waves and fluctuating effects in time can arise in a nonlinear plastic sea ice model even though the external forcing is temporally constant. The simplest example of such a wave is a "ridging front" that can occur, for example, if one pushes in one end of a series of equally separated floes (or billiard balls); the colli-

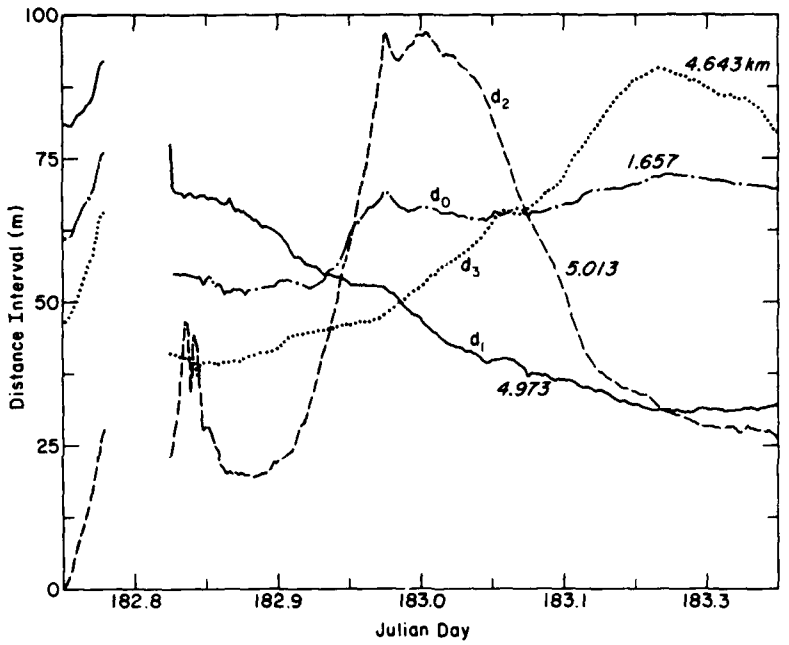

Fig. 6. Raw measured distances during a 12-hr period in the early part of the experiment. The vertical scale shows the distance scale, and absolute initial values are listed for each curve.

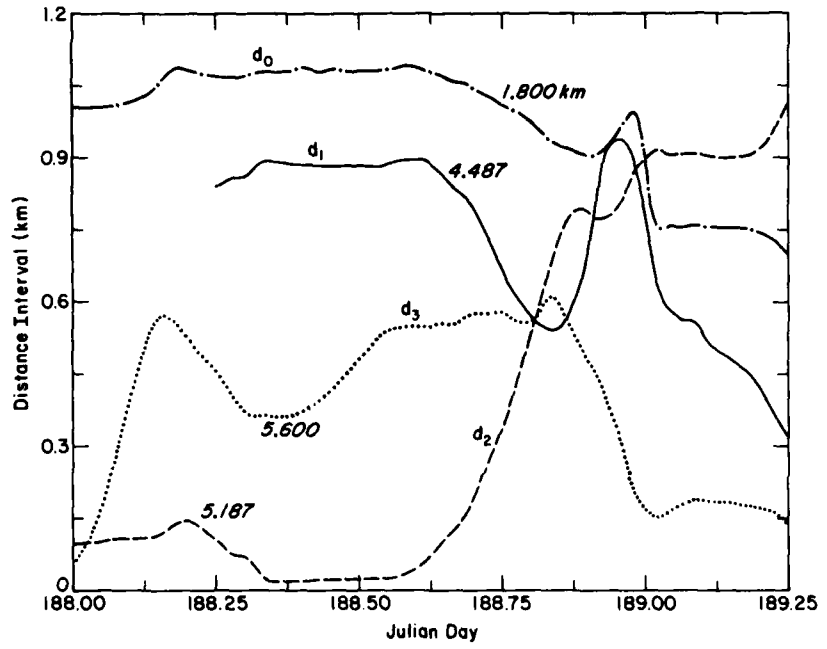

Fig. 7. Distances filtered with a low-pass filter (transition band 48- to 60-minute periods) during a 30-hr period in the late part of the experiment. The vertical scale shows the distance scale, and absolute initial values are listed for each curve.

Table 1. Positions of the Del Norte stations with respect to *Polarbjørn* in north-east coordinate system. *x* and *y* are kilometers.

Station			Bill		Ola		Cyclesonde		Jamie	
Mo	Day	Hr (GMT)	x	y	x	y	x	y	x	y
6	28	1800	-1.704	-0.153	-2.701	-4.586	-2.164	5.237	4.790	-0.584
6	29	000	-1.616	-0.213	-3.124	-3.957	-2.217	4.645	5.417	0.661
6	29	600	-1.702	-0.439	-3.206	-4.110	-2.894	3.982	4.816	-0.511
6	29	1200	-1.655	-0.473	-3.105	-4.212	-2.835	3.953	4.682	-0.405
6	29	1800	-1.676	-0.508	-3.046	-4.216	-3.139	3.766	4.820	-0.337
6	30	000	-1.717	-0.408	-3.126	-3.956	-3.364	3.735	4.884	-0.883
6	30	600	-1.714	-0.389	-3.121	-3.932	-3.329	3.777	4.848	-0.968
6	30	1200	-1.674	-0.386	-3.100	-3.962	-2.997	3.857	4.727	-0.834
6	30	1800	-1.683	-0.338	-3.051	-3.866	-3.229	3.936	4.783	-1.054
7	1	000	-1.673	-0.350	-3.091	-3.874	-3.096	3.907	4.743	-0.955
7	1	600	-1.653	-0.317	-3.148	-3.846	-3.006	3.992	4.607	-1.101
7	1	1200	-1.626	-0.306	-3.145	-3.840	-2.882	4.059	4.590	-1.098
7	1	1800	-1.631	-0.294	-3.204	-3.803	-2.876	4.106	4.399	-1.490
7	2	000	-1.631	-0.322	-3.047	-3.887	-3.016	4.123	4.483	-1.232
7	2	600	-1.638	-0.304	-3.108	-3.820	-2.932	4.097	4.527	-1.172
7	2	1200	-1.628	-0.305	-3.104	-3.825	-2.907	4.105	4.492	-1.163
7	2	1800	-1.637	-0.281	-2.985	-3.823	-3.076	4.087	4.419	-1.747
7	3	000	-1.628	-0.336	-2.887	-3.903	-3.128	3.999	4.484	-1.455
7	3	600	-1.655	-0.292	-2.986	-3.805	-3.071	4.022	4.554	-1.483
7	3	1200	-1.649	-0.287	-2.974	-3.804	-3.095	4.018	4.473	-1.638
7	3	1800	-1.679	-0.279	-2.929	-3.791	-3.218	4.048	4.555	-1.746
7	4	000	-1.663	-0.315	-2.911	-3.831	-3.198	3.965	4.418	-1.967
7	4	600	-1.688	-0.314	-2.984	-3.814	-3.153	3.904	4.400	-1.840
7	4	1200	-1.664	-0.396	-3.057	-3.914	-3.175	3.788	4.240	-1.632
7	4	1800	-1.654	-0.335	-3.211	-3.837	-3.016	3.919	4.199	-1.586
7	5	000	-1.638	-0.463	-2.975	-4.085	-3.178	3.685	4.184	-1.541
7	5	600	-1.650	-0.432	-3.239	-3.931	-3.091	3.696	4.048	-1.891
7	5	1200	-1.655	-0.386	-2.936	-4.041	-3.129	3.755	4.115	-1.846
7	5	1800	-1.595	-0.475	-2.675	-4.163	-3.459	3.632	4.318	-1.186
7	6	000	-1.572	-0.521	-2.431	-4.224	-3.725	3.474	4.448	-0.993
7	6	600	-1.576	-0.545	-2.367	-4.256	-3.800	3.375	5.283	-1.005
7	6	1200	-1.671	-0.476	-2.325	-3.879	-4.152	3.361	5.276	-1.407
7	6	1800	-1.715	-0.626	-2.208	-3.947	-4.306	2.966	5.507	-1.683
7	7	000	-1.683	-0.641	-2.149	-3.959	-4.300	2.900	5.393	-1.508
7	7	600	-1.713	-0.742	-2.075	-3.975	-4.458	2.666	5.817	-1.484
7	7	1200	-1.694	-0.808	-2.054	-4.034	-4.442	2.529	5.925	-1.097
7	7	1800	-1.686	-0.647	-2.084	-3.773	-4.653	2.787	5.872	-1.738
7	8	000	-1.598	-0.548	-2.267	-3.798	-5.094	3.142	5.329	-2.074
7	8	600	-1.443	-0.389	-1.996	-3.420	-5.210	3.180	5.365	-1.907

Table 2. Orientation of the baseline in north-east coordinate system. The angle is counted counterclockwise from the east.

Date			Angle
Mo	Day	Hr (GMT)	
6	28	1200	189.9
6	28	1800	185.1
6	29	000	187.4
6	29	600	194.5
6	29	1200	195.9
6	29	1800	196.9
6	30	000	193.4
6	30	600	192.8
6	30	1200	193.0
6	30	1800	191.4
7	1	000	191.8
7	1	600	190.9
7	1	1200	190.7
7	1	1800	190.2
7	2	000	191.2
7	2	600	190.5
7	2	1200	190.6
7	2	1800	189.8
7	3	000	191.7
7	3	600	190.1
7	3	1200	189.9
7	3	1800	189.4
7	4	000	190.7
7	4	600	190.5
7	4	1200	193.5
7	4	1800	191.4
7	5	000	195.8
7	5	600	194.6
7	5	1200	193.1
7	5	1800	196.6
7	6	000	198.2
7	6	600	199.1
7	6	1200	196.3
7	6	1800	200.1
7	7	000	200.7
7	7	600	203.4
7	7	1200	205.4
7	7	1800	200.6
7	8	000	199.4
7	8	600	195.1

sions propagate through in a manner similar to a chain-reaction auto collision. A possible example of such an event is at about 2000 GMT on 7 July (Julian day 188) in lines d_0 and d_3. Note the sudden reversal of distance in d_0 at this time after convergence had been occurring for some time in line d_3. In addition to this simple ridging front, simulations have shown that more complex propagating wave effects can arise if the coupling between the ice strength and compactness is nonlinear.

An interesting feature in the recordings was the presence of occasional sudden slips on the order of tens of meters. These effects probably arise due to an overshooting phenomenon in the ice stress that causes the distance to change rapidly and then remain approximately at a constant level. An example is shown in Figure 8, where a time series of the distance d_0 has been drawn. In days 181 and 182, four such slips occurred.

A perhaps more illustrative example of fluctuations is shown in Figure 9, which shows the relative velocities between the ship (moored to a floe) and stations O and J. These have been obtained first through central differencing the raw data and then by filtering with a low-pass symmetric filter with 241 weights and a transition band from 48- to 60-min periods (Hibler, 1972). The relative velocities are very large, with fluctuations up to 8 cm/s occurring. Since variations in the ice motion will also affect current water strings attached to ice floes, these results emphasize the necessity of making detailed ice motion measurements to properly interpret current measurements made from ice.

The stretch speed (i.e. rate of change of distance) between *Polarbjørn* and the on-ice sites was obtained very accurately with the Del Norte system. Figure 10 shows the spectra of the stretch speeds up to the frequency of 24 cycles per day. The measurement noise lies below the lowest indicated spectral density value. For sites O and J, there is a peak close to 2 cycles per day. In the higher frequencies the spectral density falls off with a red noise character. A comparison with the radar observations (Fig. 11) shows that the radar also gives the peak at about 2 cycles per day, but then the spectral density falls off much more rapidly than in the case of Del Norte data. Due to its inaccuracy it is unlikely that the radar can resolve higher frequencies than about 3 cycles per day.

Overall this data set represents a unique set of measurements of the deformation field of a series of interacting floes floating in the ocean. Because of the fine temporal resolution, accuracy of the

Table 3. Linear first order fit for the Del Norte data (6-hr displacements) in north-east coordinate system.

Date															
Mo	Day	Hr (GMT)	Dou (cm/s)	Dxu ($/H)	Dyu ($/H)	Dov (cm/s)	Dxv ($/H)	Dyv ($/H)	EI ($/H)	EII ($/H)	E_1 ($/H)	E_2 ($/H)	AE_1 (deg)	Vor (D/H)	Fit ($)
6	29	0	0.41	1.90	0.50	1.38	2.64	-2.20	-0.30	5.16	2.43	-2.73	57.2	0.61	91.8
6	29	600	-1.31	-0.49	-1.19	-2.13	-1.58	-0.93	-1.42	2.81	0.69	-2.11	-26.6	-0.11	64.7
6	29	1200	-0.01	-0.46	-0.07	0.01	0.37	0.14	-0.32	0.66	0.17	-0.49	48.8	0.13	99.9
6	29	1800	-0.08	0.53	-0.76	-0.12	0.34	-0.38	0.14	1.00	0.57	-0.43	-69.9	0.32	98.0
6	30	0	-0.21	0.44	-0.30	-0.48	-1.40	-0.62	-0.17	2.00	0.91	-1.09	-47.1	-0.32	93.7
6	30	600	-0.01	-0.11	0.06	-0.04	-0.24	0.03	-0.07	0.22	0.08	-0.15	-40.8	-0.09	98.5
6	30	1200	0.21	-0.53	0.65	0.24	0.25	0.23	-0.30	1.18	0.44	-0.74	44.5	-0.12	91.4
6	30	1800	-0.13	0.25	-0.60	-0.11	-0.66	-0.02	0.22	1.29	0.76	-0.53	-50.2	-0.02	97.0
7	1	0	0.06	-0.13	0.36	0.09	0.24	-0.04	-0.17	0.61	0.22	-0.39	35.9	-0.04	96.6
7	1	600	-0.10	-0.29	0.32	-0.06	-0.42	0.12	-0.17	0.43	0.13	-0.30	-69.1	-0.21	96.8
7	1	1200	0.12	-0.14	0.25	0.08	-0.05	0.13	-0.01	0.33	0.16	-0.17	58.0	-0.09	89.0
7	1	1800	-0.28	-0.34	0.16	-0.43	-0.93	0.07	-0.27	0.87	0.30	-0.57	-38.1	-0.31	88.5
7	2	0	0.05	0.04	-0.63	0.29	0.69	0.17	0.21	0.14	0.17	0.03	80.9	0.38	93.7
7	2	600	0.10	0.13	0.30	0.10	0.05	-0.20	-0.07	0.47	0.20	-0.27	49.2	-0.07	90.9
7	2	1200	-0.01	-0.10	0.05	0.02	0.02	0.03	-0.08	0.15	0.03	-0.11	45.7	-0.01	97.6
7	2	1800	-0.20	-0.20	-0.59	-0.75	-1.27	0.02	-0.19	1.88	0.85	-1.03	-42.2	-0.20	84.3
7	3	0	0.08	0.01	-0.32	0.21	0.83	-0.02	-0.01	0.51	0.25	-0.26	44.7	0.33	95.9
7	3	600	0.08	0.27	0.33	0.07	-0.24	-0.17	0.10	0.45	0.28	-0.18	80.0	-0.16	96.5
7	3	1200	-0.12	-0.18	-0.07	-0.20	-0.34	-0.00	-0.18	0.45	0.13	-0.31	-32.7	-0.08	81.9
7	3	1800	-0.02	0.19	-0.35	-0.10	-0.27	0.04	0.23	0.65	0.44	-0.21	-54.5	0.02	97.7
7	4	0	-0.14	-0.34	0.00	-0.42	-0.35	-0.07	-0.41	0.44	0.01	-0.43	-4.6	-0.10	69.9
7	4	600	-0.02	0.07	0.26	0.11	0.28	-0.17	-0.10	0.58	0.24	-0.34	42.1	0.01	96.7
7	4	1200	-0.24	-0.23	0.13	0.05	0.71	-0.02	-0.26	0.86	0.30	-0.56	35.9	0.17	88.5
7	4	1800	0.06	0.03	0.67	0.28	-0.13	0.09	0.12	0.55	0.34	-0.21	50.9	-0.23	90.3
7	5	0	-0.08	-0.29	-0.84	-0.38	0.68	0.04	-0.25	0.37	0.06	-0.31	-36.5	0.43	92.5
7	5	600	-0.19	0.02	0.77	-0.39	-1.02	-0.30	-0.28	0.41	0.07	-0.34	-27.5	-0.51	91.9
7	5	1200	0.13	-0.31	-0.76	0.13	0.22	0.35	0.04	0.85	0.45	-0.41	-59.0	0.28	84.2
7	5	1800	0.05	0.23	-1.26	0.66	1.80	-0.03	0.20	0.59	0.40	-0.20	56.0	0.88	94.2
7	6	0	0.02	0.18	-1.07	0.04	0.66	-0.14	0.04	0.53	0.28	-0.24	-53.7	0.50	99.9
7	6	600	1.08	1.82	-0.08	-0.15	0.11	-0.11	1.70	1.93	1.82	-0.12	89.5	0.05	84.0
7	6	1200	-0.45	0.26	-0.78	-0.28	-1.22	-1.06	-0.80	2.39	0.79	-1.59	-38.5	-0.13	95.7
7	6	1800	0.14	0.43	-0.53	-0.94	-0.15	-0.70	-0.27	1.52	0.52	-0.79	-57.2	0.11	66.4
7	7	0	-0.10	-0.31	-0.21	0.13	0.40	-0.03	-0.34	0.34	0.00	-0.34	0.8	0.17	95.5
7	7	600	0.36	0.86	-0.35	-0.33	0.27	-0.40	0.46	1.26	0.86	-0.40	-87.3	0.18	92.3
7	7	1200	0.18	0.16	0.02	0.25	0.90	0.08	0.24	0.92	0.58	-0.34	51.8	0.25	95.6
7	7	1800	-0.33	0.09	-0.38	-0.28	-1.66	-0.57	-0.48	2.14	0.83	-1.31	-39.2	-0.37	96.1
7	8	0	-1.20	-0.56	-0.66	0.09	-0.83	0.63	0.07	1.90	0.99	-0.92	-52.9	-0.05	57.0
7	8	600	0.07	-0.31	-1.05	0.44	-0.31	-1.02	-1.32	1.53	0.11	-1.43	-8.9	0.21	88.5

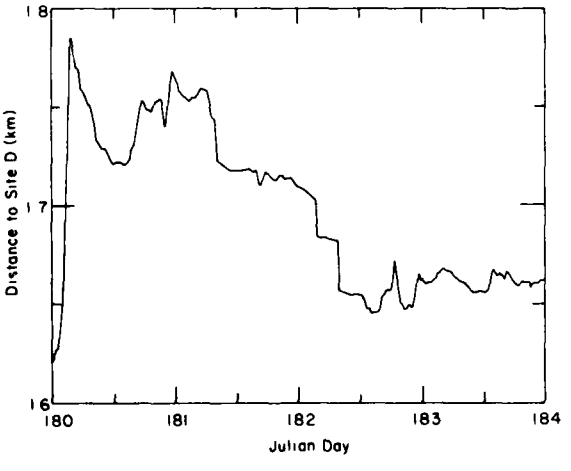

Fig. 8. Illustration of slips in the distance d_o (raw data).

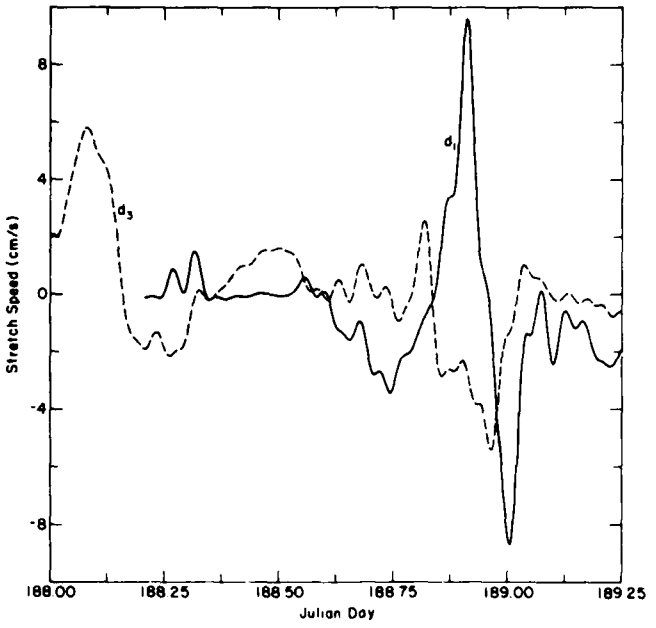

Fig. 9. Rate of change of the distances d_1 *and* d_3 *during 30 hours in late part of the experiment. The time series has been filtered with a low-pass filter (transition band 48- to 60-minute periods).*

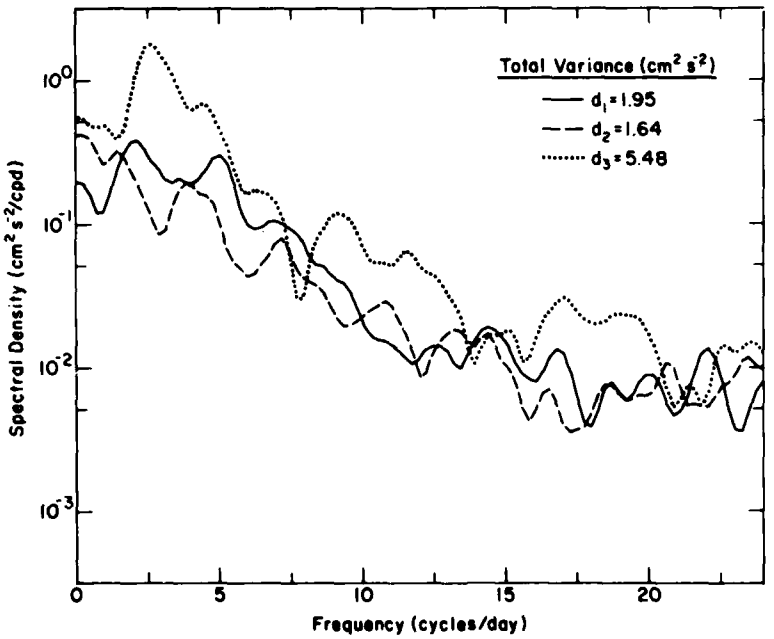

Fig. 10. The spectra of the rate of change of the distances d_1, d_2, *and* d_3.

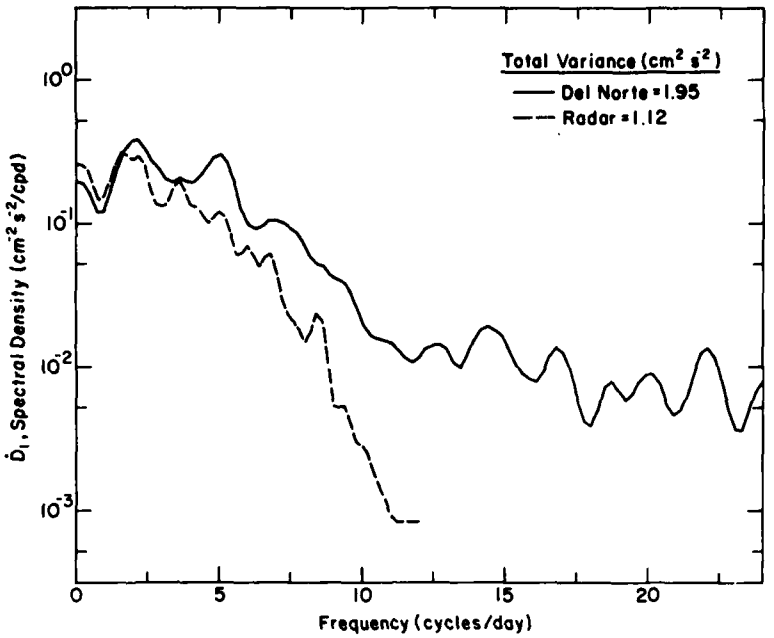

Fig. 11. The spectra of the rate of change of the distance d_l *as measured with the Del Norte system and by using the ship's radar.*

measurements, and coincidence of current and wind measurements, this data should greatly aid in sorting out the physics of marginal ice zone ice dynamics and kinematics. Such efforts are currently in progress.

REFERENCES

Hibler, W.D., III, Design and maximum error estimation for small error low pass filters, USA Cold Regions Research and Engineering Laboratory, Hanover, N.H., CRREL Research Report 304, 1972.

Hibler, W.D., III, W.F. Weeks, A. Kovacs, and S.F. Ackley, Differential sea-ice drift. I. Spatial and temporal variations in sea ice deformation, *J. Glaciol., 13,* 437–455, 1974.

Hibler, W.D., III, I. Udin, and A. Ullerstig, On forecasting mesoscale ice dynamics and buildup, *Annals of Glaciology, 4,* 110–115, 1983.

On the Rheology of a Broken Ice Field Due to Floe Collision

HAYLEY SHEN
Clarkson University
Potsdam, New York

W.D. HIBLER III
U.S. Army Cold Regions Research and Engineering Laboratory
Hanover, New Hampshire 03755-1290

M. LEPPARANTA
Institute of Marine Research
Helsinki, Finland

Stresses due to ice/ice interactions have been modeled to obey a plastic constitutive law (Hibler, 1979) or a Newtonian viscous constitutive law (Kulakov et al., 1979). The applications of these models have successfully explained long-term, overall ice motion in the Greenland Sea and the Baltic Sea (e.g. Hibler, 1979; Lepparanta, 1981).

However, near the ice edge floe characteristics are different from the interior pack ice. As a consequence, while observed mesoscale ice edge phenomena [for instance, the occurrence of ice-edge jets (Johannessen et al., 1983)] can be reproduced by ideal plastic constitutive laws through transient adjustment states (Lepparanta and Hibler, 1985), it is desirable to understand ice rheology in the marginal ice zone from a more fundamental point of view.

During MIZEX 83, a considerable amount of precision ice deformation data (Hibler and Lepparanta, 1984) were obtained. These data provide a basis for sorting out the physics that governs the ice rheology in the MIZ.

The deformation data, together with other MIZEX 83 observations, show that in the MIZ the moving ice field consists of a granular material with various sizes, shapes, and thicknesses. This material undergoes a deformation that is quite chaotic when a fine temporal-resolution record is studied. Ice floes fluctuate from their mean positions and collide with neighboring ones without forming ridges. The frequency of these occurrences is in the order of 10/day. Assuming the average floe in the MIZ has a diameter of 50 m and a thickness of 1 m, and the ice compactness is about 0.8, the collisional momentum transfer rate is then of the order of 1 dyne/cm. This magnitude is comparable with other forcing mechanisms that exist in the field. Hence, it is of considerable interest to analyze the internal stresses as a result of the collisional ice interactions.

In this note we outline a preliminary theory for determining the rheology of a broken icefield due to floe collisions. The theory, which is based on an idealized granular flow concept, quantifies the deformation-induced velocity fluctuations as well as the internal stresses. Initial comparison of the theoretical velocity fluctuations are then made with the field data obtained in MIZEX 83.

Consider two disks, A and B, embedded in a deforming ideal granular material, as shown in Figure 1. When these two disks collide, the amount of momentum transfer depends on their relative velocity and their material properties as characterized by density ρ_s, the restitution coefficient ϵ, and the frictional coefficient μ.

For a given deformation tensor

$$\begin{pmatrix} \partial u/\partial x & \partial u/\partial y \\ \partial v/\partial x & \partial v/\partial y \end{pmatrix} \tag{1}$$

the relative velocity between A and B is

$$V_{AB} = D\left(\frac{\partial u}{\partial x}\cos\theta + \frac{\partial u}{\partial y}\sin\theta\right)i + D\left(\frac{\partial v}{\partial x}\cos\theta + \frac{\partial v}{\partial y}\sin\theta\right)j + \sqrt{2}\,v' \tag{2}$$

where v' is an isotropic random fluctuation component of a single disk. After the collision, from linear momentum conservation and energy loss due to friction and incomplete restitution, the momentum transfer can be obtained as

$$\begin{aligned}\Delta M_B = m_s D\left(\frac{1+\epsilon}{2}\right)\Bigg|\Bigg[&(\cos^3\theta - \mu\cos^2\theta\sin\theta)\frac{\partial u}{\partial x} + (\sin\theta\cos^2\theta - \mu\sin^2\theta\cos\theta)\left(\frac{\partial u}{\partial y} + \frac{\partial v}{\partial x}\right) \\ &+ (\cos\theta\sin^2\theta - \mu\sin^3\theta)\frac{\partial v}{\partial y}\Bigg]i + \Bigg[(\sin\theta\cos^2\theta + \mu\cos^3\theta)\frac{\partial u}{\partial x} \\ &+ (\sin^2\theta\cos\theta + \mu\sin\theta\cos^2\theta)\left(\frac{\partial u}{\partial y} + \frac{\partial v}{\partial x}\right) + (\sin^3\theta + \mu\cos\theta\sin^2\theta)\frac{\partial v}{\partial y}\Bigg]j\Bigg| \\ &+ m_s\sqrt{2}\,v'\sin\alpha N\end{aligned} \tag{3}$$

After statistically averaging all possible collision arrangements taking place between A and B,

$$\Delta\bar{M}_B = m_s D\,\frac{1+\epsilon}{3\pi}\left|\left[(2+\mu)\frac{\partial u}{\partial x} + (1+2\mu)\frac{\partial v}{\partial y} - \frac{4\sqrt{2}}{\pi^2}v'\right]i\left[\tfrac{1}{2}(1-\mu)\left(\frac{\partial u}{\partial y} + \frac{\partial v}{\partial x}\right)\right]j\right| \tag{4}$$

for case 1 in Figure 1, and

$$\Delta\bar{M}_B = m_s D\,\frac{1+\epsilon}{3\pi}\left|\left[\tfrac{1}{2}(1-\mu)\left(\frac{\partial u}{\partial y} + \frac{\partial v}{\partial x}\right)\right]i + \left[(1+2\mu)\frac{\partial u}{\partial x} + (2+\mu)\frac{\partial v}{\partial y} - \frac{4\sqrt{2}}{\pi^2}v'\right]j\right| \tag{5}$$

for case 2 in Figure 1.

The stress tensor generated by these collisions is modeled as the rate of total momentum transfer across a surface defined by all disks B that occupy the unit control surface. Hence

$$\tau_{ij} = p_i \cdot f \cdot \Delta M_j \tag{6}$$

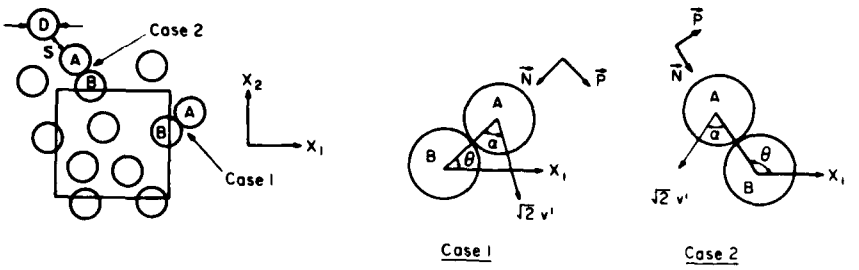

Fig. 1. A deforming field of disks and two blow-up cases for a given deformation tensor.

where p_i = number of disks on a unit surface = p (if isotropic distribution)
$f = v'/2S$; S = average gap size (7)
ΔM_j = x_j component of ΔM_B

Substituting (4) and (5) into (6), we obtain

$$\underline{\tau} = m_s \frac{1+\epsilon}{2} \cdot f \cdot p \cdot \left\{ \frac{2D}{3\pi} [(1+2\mu)(Tr\underline{D})\,\underline{I} + (1-\mu)\underline{D}] - \frac{4\sqrt{2}}{\pi^2} v' \underline{I} \right\} \tag{8}$$

The fluctuation component v' has to do with the energetics of the deforming granular material. Stronger deformation induces more frequent collisions, hence a higher v'. Higher v' increases the frequency of collisions. Each collision involves three basic dissipation mechanisms: that due to moving through the surrounding fluid, that due to an incomplete restitution after a collision, and that due to the frictional force between disks during contact. These dissipations damp out collisional energy and reduce v'. Assuming the time needed to adjust the value of v' to a gradually changing deformation field is short, balance between the deformational increase and the collisional damping of v' can be arrived at instantaneously. Therefore,

$$\underline{\tau} \cdot \underline{D} = \frac{p}{D} \cdot f \cdot E \tag{9}$$

where $\underline{D}$ is the strain tensor and E is the average energy loss per collision. The energy loss due to a collision shown in Figure 1 is

$$\tfrac{1}{2} m_s [V_A^2 + V_B^2 - V_A^{*2} - V_B^{*2}] + S C_D \varrho_f D d v'^2 \tag{10}$$

where * denotes post-collision conditions. Again averaging throughout all possible collision arrangements, we obtain

$$E = \frac{m_s D}{4} [(1-\epsilon^2) - \mu^2 (1+\epsilon)^2] \left\{ \tfrac{3}{8} \left(\frac{\partial u}{\partial x} + \frac{\partial v}{\partial y} \right)^2 + \tfrac{1}{2} \left[-\frac{\partial u}{\partial x} \frac{\partial v}{\partial y} + \tfrac{1}{4} \left(\frac{\partial u}{\partial y} + \frac{\partial v}{\partial x} \right)^2 \right] \right\}$$

$$+ m_s \frac{v'^2}{D} \left[\frac{1-\epsilon^2}{4} + \frac{\mu(1+\epsilon)}{\pi} - \frac{\mu^2 (1+\epsilon)^2}{4} + \frac{4}{\pi} \frac{C_D S}{D} \frac{\rho_f}{\rho_s} \right] \tag{11}$$

Substituting (8) and (11) into (9), we obtain an equation for v' as the following:

$$k_1 v'^2 + k_2 v' + k_3 = 0 \tag{12}$$

where

$$k_1 = 2\left[\frac{1-\epsilon^2}{4} + \frac{\mu(1+\epsilon)}{\pi} - \frac{\mu^2(1+\epsilon)^2}{4} + \frac{4}{\pi}\frac{C_D S}{D}\frac{\rho_f}{\rho_s}\right]$$

$$k_2 = \frac{4\sqrt{2}}{\pi^2} D I_1$$

$$k_3 = \frac{D^2}{2}\left[1-\epsilon^2-\mu^2(1+\epsilon)^2\right]\left(\tfrac{3}{8}I_1^2 - \tfrac{1}{2}I_2\right) - (1+\epsilon)\frac{2D^2}{3\pi}\left[(2+\mu)I_1^2 - 2(1-\mu)I_2\right]$$

$$I_1 = \frac{\partial u}{\partial x} + \frac{\partial v}{\partial y}\,; \quad I_2 = \frac{\partial u}{\partial x}\frac{\partial v}{\partial y} - \tfrac{1}{4}\left(\frac{\partial u}{\partial y} + \frac{\partial v}{\partial x}\right)^2 \tag{13}$$

The above quadratic equation for v' can be solved if the material properties ϱ_f, ϱ_s, ϵ, μ, and the fluid drag coefficient C_D are given, and the disk size D, average gap size S, and deformation invariants I_1 and I_2 are provided.

For MIZEX 83 ice data, the material properties are estimated as $\varrho_s/\varrho_f = 0.9$, $\epsilon = 0.2$, $\mu = 0.2$, $C_D = 0.5$, $D = 50$ m, and $S = 5$ m (which corresponds to a compactness of 0.8). The expected v' from the theory is

$$v_s' = D\{-0.39I_1 + \sqrt{0.69I_1^2 - 0.25I_2}\}. \tag{14}$$

Since $f = v'/2S$, the stress tensor may be obtained when the above is substituted into (8).

During the MIZEX 83 mesoscale ice dynamics program, the positions of four transponders relative to the ship were recorded at 3-min intervals (Hibler and Leppäranta, 1984). The data were then filtered through a low-pass filter of transition band 48–60 minutes. Adopting the Del Norte coordinate system, the velocity field was then computed and resampled at half-hour frequency. This velocity field is denoted here as $V_{actual}(V_a)$. Because the ship was used as a reference point in the Del Norte system V_s of the ship is zero.

A linear first-order fit procedure is then adopted to obtain the ship's velocity (V_s) and the components in the deformation tensor ($\partial u/\partial x$, $\partial u/\partial y$, $\partial v/\partial x$, $\partial v/\partial y$). This deformation tensor and the filtered position data for the four transponders are then utilized to give the strain-predicted velocity at the transponders' and the ship's locations. These velocity data are denoted here as $V_{Linear\ fit}(V_{tf})$. These strain-predicted velocities are viewed as the mean velocities of the four transponders.

Let

$$V_a = u_a i + v_a j$$

$$V_s = u_s i + v_s j$$

$$V_{tf} = u_{tf} + v_{tf} \tag{15}$$

in the Lagrangian coordinate system. The actual velocities of the transponders and the ship are

$$V_a^L = V_a - V_s = (u_a - u_s)i + (v_a - v_s)j \qquad \text{for the transponders}$$

$$V_s^L = -V_s = -u_s i - v_s j \qquad \text{for the ship} \tag{16}$$

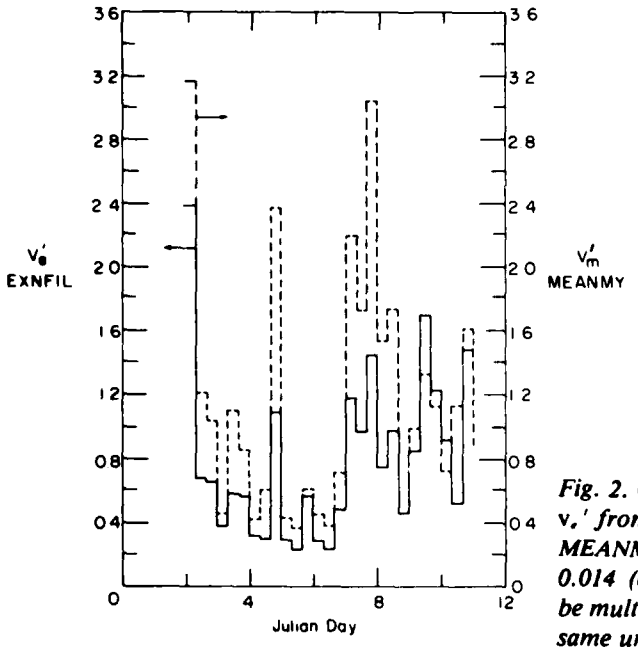

Fig. 2. Comparison of fluctuations. v_e' from file EXNFIL, v_m' from file MEANMY. A conversion factor of 0.014 (cm/sec)/[cm(%/hr)] has to be multiplied to v_e' to put it into the same unit as v_m'.

and the linear fit or the mean velocities of the transponders and the ship are

$$\mathbf{V}_{tf}^L = \mathbf{V}_{tf} - \mathbf{V}_e = (u_{tf} - u_e)\mathbf{i} + (v_{tf} - v_e)\mathbf{j} \qquad \text{for the transponders}$$

$$\mathbf{V}_{tf} = 0 \qquad \text{for the ship.} \tag{17}$$

The velocity fluctuation from measured data is obtained as

$$v_m' = \tfrac{1}{5} \Sigma \, |\mathbf{V}_e^L - \mathbf{V}_{tf}^L|. \tag{18}$$

The above summation is taken over the four transponders and the ship.

The two velocity fluctuation data sets v_e' and v_m' are computed from (14) and (18) at half-hour intervals. These two data sets are smoothed with an 8-hr block average procedure. The data are then represented in histograms at an 8-hr step size and the correlation coefficient between the two histograms is obtained. A typical histogram presentation of the correlation between v_e' and v_m' is given in Figure 2.

Since the time series of the data have wide spectra, correlation between v_e' and v_m' is investigated under six different cases. Let

$$F_{P-Q}(\text{data}) \tag{19}$$

represent the low-pass filtered data with band width from P to Q hr. Three filtered data sets $F_{2.5\text{-}10}(I_1, I_2)$, $F_{2.5\text{-}10}(V_e^L)$, and $F_{2.5\text{-}10}(V_{tf}^L)$ are constructed. Five velocity fluctuation files are obtained with or without the filtering procedure. Table 1 illustrates how these five files are obtained.

The result of the correlation and the mean and standard deviation of pairs of histograms for v_e' and v_m' are listed in Table 2, where $D = 50$ m, $\varrho_s/\varrho_f = 0.9$, $\epsilon = \mu = 0.2$, *and* $C_D = 0.5$ are used in (14).

Table 1. Files of velocity fluctuation.

File name	*Data provided*	*Data used*
EXNFIL	(eq 14)	I_1, I_1 no filter
EXYFIL	(eq 14)	$F_{2.5\text{-}10}(I_1, I_2)$
MEANMN	(eq 18)	V_a^1, V_{lf}^1 no filter
MEANMY	(eq 18)	V_a^1 no filter, $F_{2.5\text{-}10}(V_{lf}^1)$
MEAYMY	(eq 18)	$F_{2.5\text{-}10}(V_a^1, V_{lf}^1)$

Table 2. Correlation of velocity fluctuations.

Theory	*Mean*	*S.D.*	*Field data*	*Mean*	*S.D.*	*Correlation coefficient*
EXNFIL	0.01	0.007	MEANMN	0.60	0.40	0.9
			MEANMY	1.19	0.77	0.83
			MEAYMY	0.35	0.28	0.9
EXYFIL	0.008	0.006	MEANMN			0.72
			MEANMY			0.59
			MEAYMY			0.89

The purpose of this note is to demonstrate the overall procedure for determining the rheology of a broken ice field due to floe collisions. However, for a consistent theory some modifications are needed. Most notably these equations have not included the mean flow in the determination of the rheology, which is particularly important in divergence. Also, although good correlation is obtained with the observed deformation data the observed fluctuations are larger than predicted. A more complete analysis addressing these issues is currently underway and will be submitted for journal publication in the near future.

REFERENCES

Hibler, W.D. III, A dynamic thermodynamic sea ice model, *J. Phys. Oceanogr.*, *9*(4), 815-846, 1979.

Hibler, W.D. III and M. Lepparanta, MIZEX 83 mesoscale sea ice dynamics: Initial analysis, *MIZEX Bulletin IV*, 19-28, 1984.

Johannessen, O.M., J.A. Johannessen, J. Morison, B.I Farrelly, and E.A.S. Svendsen, Oceanographic conditions in the marginal ice zone north of Svalbard in early fall 1979 with an emphasis on mesoscale processes, *J. Geophys. Res.*, *88*(C5), 2755-2769, 1983.

Kulakov, I.Yu., M.I. Maslovsky and L.A. Timokhov, Seasonal variability of Antarctic sea ice extent: Its numerical modeling, *Proc. ICSI/AIDJEX Symp. on Sea Ice Proc. and Models,* Univ. of Wash., 1979.

Lepparanta, M. and W.D. Hibler III, The role of plastic ice interaction in marginal ice zone dynamics. Submitted to *J. Geophys. Res.*

Lepparanta, M., An ice drift model for the Baltic Sea, *Tellus*, *33*(6), 583-596, 1981.

Heat and Mass Balance Observations During the MIZEX 83 Drift Program

GARY A. MAYKUT
Department of Atmospheric Sciences/Geophysics Program
University of Washington
Seattle, Washington

INTRODUCTION

The summer decay and retreat of the marginal ice zone is controlled by a variety of complex interactions taking place among the ice, ocean and atmosphere. Melting alters not only the properties of the ice cover, but also the structure of the upper ocean. Horizontal gradients in meltwater input and the proximity of warmer and more saline water can give rise to a variety of mesoscale phenomena in the ocean, while floe breakup and increasing stratification beneath the ice affect the response of the ice to winds and currents and the rate at which heat is transferred from the water to the ice. Both the atmosphere and ocean supply energy needed to drive the melt. The primary source of energy from the atmosphere is shortwave radiation, and the properties of the ice which affect its absorption and distribution must be considered as important variables in the system. Heat transfer from the water to the ice occurs at both the edges and bottoms of floes and is a major factor in the summer decay cycle. Much of the heat supplied to the ice by the water appears to be absorbed shortwave radiation which enters the upper ocean through leads and areas of thin ice. However, the rate at which this heat is lost to the ice is complicated by lateral advection of ice and water across the edge, mixed layer stratification, waves, floe interactions and mesoscale circulations associated with the MIZ. Quantitative information on the role of these processes is meager.

At present we are unable to answer many basic questions regarding the heat and mass balance of the summer MIZ. For example, what is the relative importance of the atmosphere and ocean in the decay cycle? What fraction of the mass loss occurs at the extreme ice edge? How is solar energy absorbed in the water partitioned between lateral melting, bottom ablation, temporary storage in the ocean, and loss to the atmosphere? What are the dominant processes involved in the transport of heat from the water to the ice? To what extent does freshwater input from the melting ice retard the vertical exchange of heat with the deeper ocean? How does ice movement and proximity to the edge affect heat transport and density structure in the summer mixed layer? To answer such questions requires concurrent data on the state of the ice (concentration, thickness, floe size distribution, snow and pond coverage), mass changes at floe boundaries, energy input to the ice and ocean, ice movement, ocean structure, and heat exchange processes between system components. Although the program outlined below is concerned primarily with temporal changes in the heat and mass balance of the ice pack, it should provide information needed for at least a preliminary examination of many of the above questions. Because shortwave radiation is a principal agent in the decay cycle, the work has a strong focus on properties and processes that affect its interaction with the ice and upper ocean.

EXPERIMENTAL PROGRAM

Our overall plan for MIZEX 83 was to instrument a few typical floes in the MIZ and to monitor mass changes occurring at the top, bottom and sides of these floes. Other measurements included incoming radiation, ice thickness, snow depth, pond coverage, internal ice temperatures, radiative properties, and heat content changes in leads.

We plan to use these data to determine the relative importance of the various energy sources and to construct local heat and mass budgets for the individual floes. With these local budgets and estimates of ice concentration and pond coverage derived from aerial photography it should ultimately be possible to obtain area-integrated totals for the region. Of particular concern in the study was the input of solar energy to the ocean and the factors that control its transfer to the ice. Analysis of the above data in conjunction with results from the oceanographic program should yield detailed information on the role of the upper ocean in the decay and retreat of the ice and allow us to gauge its importance in relation to atmosphere-ice interactions.

Heat and mass balance observations during the drift phase were concentrated on two floes ("Tent" Floe and "Spot" Floe) located about 150 m south of the *Polarbjørn*. Tent Floe, measuring about 25×75 m in the horizontal, averaged 1.9 m in thickness and was composed largely of first-year ice. The somewhat thicker (2.4 m) Spot Floe measured about 50×75 m and appeared to contain areas of both first-year and second-year ice. Eleven hot wire thickness gauges were installed in these two floes to monitor mass changes at the bottom of the ice. An additional four gauges were placed in the ice next to the ship to see to what extent waste heat from the ship might affect the melting. Surface ablation was measured at 27 sites on these three floes. Wall profiles and observations of edge erosion were made at several locations around Tent Floe. Salinity and temperature profiles, taken in leads during the drift and ice edge phases, were used to calculate the heat content of the upper several meters of the water column. Total incoming shortwave and longwave radiation fluxes were monitored continuously over the ice on Tent Floe throughout the drift period. Complementary data on the effect of cloudiness on the spectral distribution of incident irradiance were also obtained. Spectral and total albedo measurements were made over bare multiyear ice, snow, ponds, and thin first-year ice. Conductive heat fluxes in the ice were estimated from internal temperature data in Spot Floe.

RESULTS

Conditions during the drift phase were unexpectedly quiescent—ice concentration was high, leads and floes were small, wave action was minimal and there was little in the way of floe breakup or mechanical erosion. Because the drift took place early in the melt season, albedos were still high, slowing the surface melt and producing only a slight freshening of the upper ocean. Ice decay was probably close to the minimum amount that can be expected in the summer MIZ. Many floes in the region contained significant amounts of algae and dirt, lowering their albedos and increasing the amount of shortwave energy absorbed. Offsetting this effect, however, was the small melt pond coverage on the thicker (> 1 m) floes, which caused them to have somewhat higher albedos than similar ice in the central pack or in coastal areas. Floes thinner than 1 m tended to be quite smooth and were frequently covered almost entirely by shallow ponds. Some large multiyear floes with pond coverage typical of the central Arctic were sighted during aircraft overflights, but were unusual. The great majority of floes in the vicinity of the ship appeared to be similar in character to Spot and Tent Floes.

Bottom ablation

Daily ablation totals at each of the thickness gauge sites are given in Table 1. Cumulative bottom ablation over the experimental period is sketched in Figure 1. Average melt rates varied between 5 and 9 mm/day. Standard deviations were large. Part of the explanation for the large deviations was a definite tendency for thicker ice to ablate more rapidly. Figure 2 shows the average melt

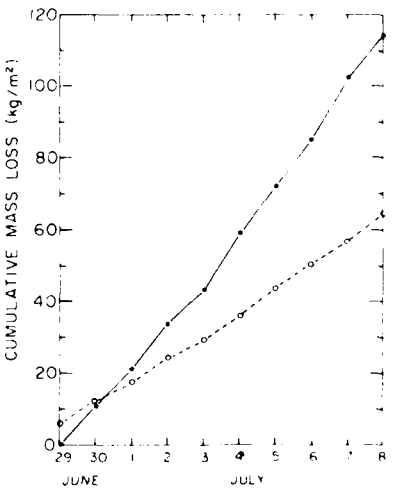

Fig. 1. Cumulative mass losses occurring at the top (solid curve) and bottom (dashed curve) of floes near the Polarbjørn *during the drift phase.*

Table 1. Bottom ablation (mm/day) on floes near the *Polarbjørn* during the drift phase. Gauges D1–D3 were located on "Dirty Floe" adjacent to the ship; gauges T1–T6 were located on "Tent Floe," the site of the mixed layer studies; and gauges S1–S5 were located on "Spot Floe." h_o was the initial ice thickness when the gauges were installed. The negative value at S5 on 5 July is the result of meltwater input beneath the ice causing formation of a false bottom.

Gauge No.	h_o (m)	June 29	June 30	July 1	July 2	July 3	July 4	July 5	July 6	July 7	July 8	TOTAL
D1	2.00	6	11	13	14	4	6	3	3	10	10	82
D2	1.85		6	6	18	3	4	7	6	5	5	60
D3	1.77		5	7	7	6	5	9	8	3	4	54
S1	2.86			9	9	10	15	20	20	20	20	123
S2	1.56			5	6	6	6	7	4	6	5	45
S3	2.11			11	11	3	8	10	4	6	6	59
S4	2.77			5	5	3	15	14	1	5	19	67
S5	1.72			2	3	5	5	-13	8	2	6	18
T1	2.47			2	3	11	3	11	1	15	4	50
T2	1.51			3	2	3	1	11	3	1	0	24
T3	1.50					1	6	9	8	3	5	32
T4	2.57					6	6	14	16	3	13	58
T5	2.67					7	7	17	11	10	20	72
T6	1.77					6	8	6	11	6	4	41
Mean		6.0	7.3	6.3	7.8	5.3	6.8	8.9	7.4	6.8	8.6	7.1
Standard deviation			3.2	3.7	5.2	2.8	3.9	7.8	5.6	5.3	6.7	4.9
Number of gauges		1	3	10	10	14	14	14	14	14	14	

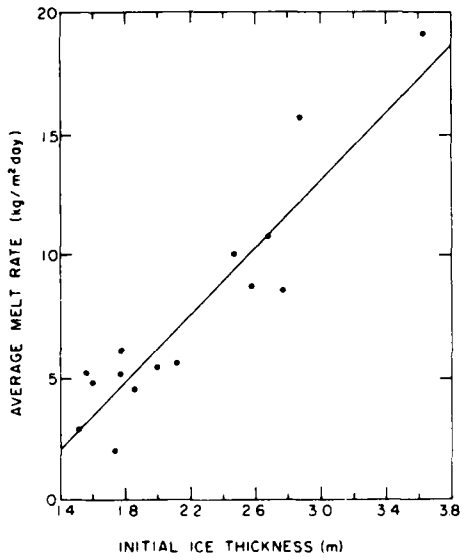

Fig. 2. Average melt rate at the bottom of the ice vs initial ice thickness during the period 3–8 July 1983.

rate ($\bar{f}$) over the final six days of the drift plotted against the initial ice thickness (h_o). The solid line in Figure 2 represents a least squares fit to the data: $\bar{f} = -7.64 + 6.9 h_o$ ($R^2 = 0.83$). A strong dependence of $\bar{f}$ on h was not expected over such a small thickness range and we are unsure as to the reason. The two largest values of $\bar{f}$ were measured in small ridge keels, but thickness measurements were not sufficiently dense to provide a good definition of bottom roughness. Despite the relatively small amount of bottom melting, ablation rates were still much larger than those observed in areas of perennial ice.

Snow cover and surface ablation

Although melting at the upper surface was already in progress, a substantial amount of snow still covered the ice at the beginning of the drift. Measurements from a 121-point survey grid (Table 2) showed snow thicknesses varying between 0 and 123 cm, with an average of 43.3 cm. Snow density remained essentially constant throughout the period at 400 kg/m³. Surface ablation totaled about 115 kg/m² during the period (Figure 1), a

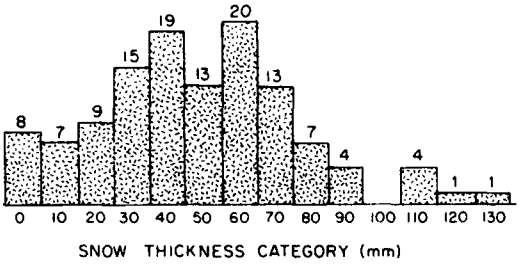

Fig. 3. Histogram of snow depths near Polarbjørn, *27 June 1983.*

mass loss roughly double that observed on the underside of the ice. Daily ablation amounts are tabulated for each of these sites in Table 3. Area-weighted surface melt rates for bare ice, snow-covered ice, and the combined average are presented in Figure 4. The decreasing rate of meltwater generation by the snow and the corresponding increase by the ice simply reflect changes in the relative area covered by snow and bare ice.

The heavy snow cover encountered in the MIZ was in striking contrast to regions of perennial ice and to coastal portions of the Arctic Basin where snow typically vanishes by 1 July. Extensive snow cover was also noted three weeks later in the Greenland Sea during the transect of the *Polarstern* to the Greenland coast. At this point it is difficult to be certain whether lower energy input at the surface or greater snowfall was primarily responsible for the large amounts of snow, but we

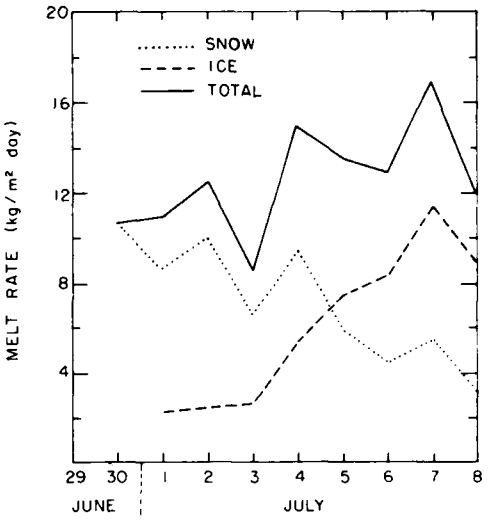

Fig. 4. Area-weighted melt rate averages at the surface of the ice cover during the drift phase. Solid curve represents total rate of mass loss, while the dashed and dotted curves represent the respective contributions from ice and snow to the total.

suspect the latter. The significance of the extensive snow cover is that it reduces the absorption of solar radiation and protects the surface of the ice from erosion. This slows the decay cycle and means that heat from the water must be a major factor in the retreat of the MIZ during early summer.

Table 2. Snow depth (mm) survey taken on rough 2nd year floe near *Polarbjørn*, 27 June 1983. Grid spacing was 3 m. Melting was in progress and the snow was nearly isothermal. Mean snow depth was 433 mm with a standard deviation of 274 mm.

205	0	580	565	105	85	1105	460	455	620	230
350	55	575	65	370	230	595	320	460	0	730
0	50	420	455	170	460	470	575	565	605	585
625	0	360	245	395	605	605	775	340	490	735
305	460	210	510	220	0	1230	295	175	135	780
360	280	400	900	660	110	740	30	0	0	1050
825	345	625	845	585	520	530	640	665	775	0
500	610	705	1085	1090	885	590	470	505	505	620
440	1065	605	360	260	255	205	190	250	515	700
0	475	345	365	215	250	255	185	390	530	595
340	680	365	330	170	210	95	305	365	510	515

Table 3. Summary of surface ablation (mm) measurements made during the drift phase. Daily mean mass losses are given in kg/m² and specific loss rates in kg/m² day. A "/" beside a number indicates a transition from snow-covered to bare ice, values to the right of the slash representing ice ablation and those to the left snow ablation.

	June	July								Specific
Stake	30	1	2	3	4	5	6	7	8	Loss Rate
D1	31	32	42	35	40	27	28	50	20	11.3
D2	32	32	38	28	35	33	32	/20	8	12.0
D3	32	32	46	15	47	31	32	/18	20	13.2
D4	20	20	21	30	30	27	28	35	20	9.4
D5	37	37	45	15	47	34	34	55	35	13.9
D6	22	23	/6	20	27	19	19	5	35	15.1
S1		/20	23	23	30	16	12	27	13	19.0
S2		15	19	/5	17	13	12	24	26	13.0
S3		6	9	11	/11	18	17	27	7	10.6
S4		/21	26	17	15	5	25	20	24	18.7
S5		/13	16	11	18	9	15	17	18	13.9
A1		48	33	27	50	23	17	40	35	12.7
A2		30	40	26	40	/15	12	40	23	16.6
A3		21	37	24	43	33	25	50	13	11.5
A4		33	20	27	30	35	25	35	50	11.8
A5		32	35	12	40	27	33	35	32	11.5
A6		32	32	16	49	28	32	35	19	11.3
A7		20	32	25	35	32	11	/11	9	9.4
A8		22	31	29	41	/22	33	16	0	13.7
A9		28	38	23	/22	22	11	17	11	13.7
A0		30	35	19	/24	24	14	19	10	14.4
T1			25	30	/13	9	18	27	3	11.3
T2			25	27	43	25	/9	14	7	9.8
T3			39	16	44	25	33	/12	14	11.0
T4					15	13	18	20	11	13.4
T5					25	27	/16	17	9	10.3
T6					30	/10	20	16	12	11.5
Mean mass loss	11.6	11.8	13.4	10.3	16.4	13.0	13.3	17.5	12.1	
Standard deviation	2.6	4.2	4.8	4.4	4.2	4.0	5.0	6.1	7.1	
Number of stakes	6	21	24	24	27	27	27	27	27	

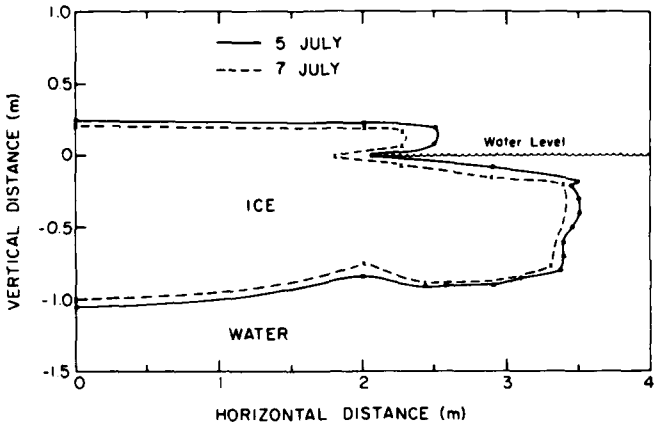

Fig. 5. Ice wall profiles taken on the edge of Tent Floe on 5 and 7 July.

Lateral erosion

Ice wall profiles measured on Tent Floe were of two general types: 1) those shaped primarily by thermal processes, which had an underwater ledge, frequently accompanied by an overhanging lip above the waterline, and 2) those shaped by mechanical erosion from floe interactions, which were more vertical and lacked the underwater bulge. Undercutting on the MIZEX floes was substantially less than the amount we observed during July 1982 in the dynamically active MIZ west of Prince Patrick Island. Figure 5 shows two profiles taken on 5 and 7 July. Despite the small wave activity, the rate of mass loss was large when compared to those at the top and bottom of the floe. Horizontal retreat of the vertical ice wall below the water was about 5 cm/day, while retreat of the sloping underwater "ramp" averaged 20–30 cm/day. Horizontal retreat of the notch at the waterline was 12 cm/day, roughly the same as that of the overhanging lip. At the start of the observational period, the leads contained a great deal of ice debris, which was probably generated as a result of floe jostling by the ship. This debris melted rapidly during the first two days. Little debris was sighted after this period, indicating that mechanical erosion on floe edges was minimal.

Melt pond and bare ice coverage

Melt pond coverage was much less than that observed in the central Arctic or in coastal regions. Pond area reached a maximum of about 20% for 1-2 days, then decreased rapidly to about 5% by 8 July (Figure 6). The reason for the smaller coverage was the smaller size of the floes, which made it relatively easy for meltwater to find a path to the ocean. An exception to this was the thin (< 1 m) floes, which were flat, and whose surfaces were close to the waterline. Such floes tended to be covered by extensive but very shallow ponds. Since the more heavily ponded multiyear floes were not a significant factor, surface meltwater storage was low, and freshwater input to the ocean in the drift area should be closely correlated with measured ablation.

Figure 6 also shows the relative area covered by bare ice, based on data from the surface ablation

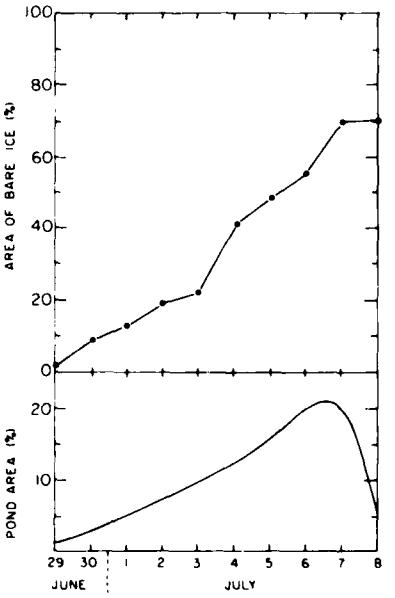

Fig. 6. Relative area covered by ponds and bare ice during the drift phase.

array. Because stakes were frequently located in higher areas, these values may be somewhat biased toward areas of bare ice. It should be remembered, however, that values for pond and bare ice areas apply only to the three instrumented floes. Aerial photos in the vicinity of the ship disclose numerous thin pond-covered floes, so when regional totals are ultimately obtained, they will probably indicate less snow and greater pond coverage.

Internal ice temperatures

To determine if there was any significant conduction of heat within the ice, temperatures were measured at five levels in 3-m ice near a thickness gauge in the middle of Spot Floe. The results (Table 4) indicate that temperatures in the lower meter of the ice were essentially isothermal. Temperatures in the upper portion of the ice tended to be more variable, reflecting differences in cloudiness and air temperature on the different days. Although there was slight warming over the nine-day period, heat conduction near the bottom of the ice was small, and bottom ablation rates should provide a direct measure of the oceanic heat flux.

Table 4. Internal ice temperatures (°C) measured at the center of Spot Floe during the drift phase. Initial ice thickness was 2.97 m.

	Depth (meters)				
Date	0.75	1.75	2.00	2.25	2.50
30 June	-0.68	-2.06	-2.23	-2.21	-2.20
2 July	-0.97	-1.59	-2.21	-2.20	-2.21
3 July	-0.84	-1.42	-2.17	-2.16	-2.18
4 July	-0.71	-1.53	-2.11	-2.11	-2.13
5 July	-0.64	-1.59	-2.10	-2.08	-2.08
7 July	-0.47	-1.43	-2.00	-2.00	-2.02
8 July	-0.53	-1.49	-1.97	-1.95	-2.00

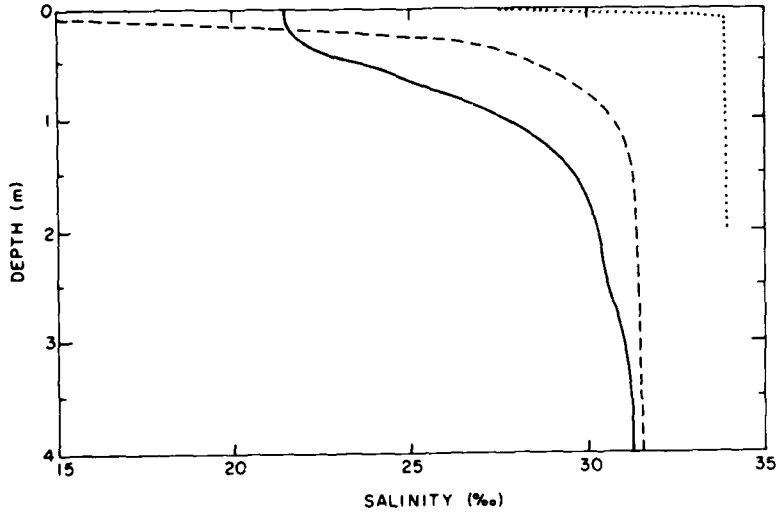

Fig. 7. Comparison of salinity profiles taken in leads at three sites during the drift and ice edge phases. Site A (dotted curve) was a 25-m-wide lead adjacent to Spot Floe on 3 July; Site B was a 3- to 4-m-wide lead in a region of 50% ice concentration on 21 July (dashed curve); and Site C (solid curve) was on the windward side of a 50-m-wide lead in a region of low ice concentration on 22 July.

Heat content of leads

To obtain information on the distribution of heat in leads, CTD profiles were taken in the upper 2-4 m of the water column using hand-held Seabird temperature and conductivity cells. Results are summarized in Figures 7-9. Measurements during the drift phase were made on 3 July in a 25-m-wide rectangular area of open water adjacent to Spot and Tent Floes. Profiles were taken in the center of the lead, as well as on the upwind and downwind sides. Although the heat content of the lead was about 15% larger on the downwind side, profiles were similar at all three sites, showing a lower salinity meltwater layer in the upper 10-20 cm. There was no evidence of meltwater entrainment below this level. Ice concentration at this time was about 85%, and the cumulative melting, averaged over the region, totaled about 60 kg/m^2. Heat content in the lead was 20-25% of the daily solar input, indicating rapid transport of heat to the walls and/or under the ice.

CTD data were also gathered in several leads further south (79°30′) during the ice edge phase. On 21 July six profiles were taken in an area of

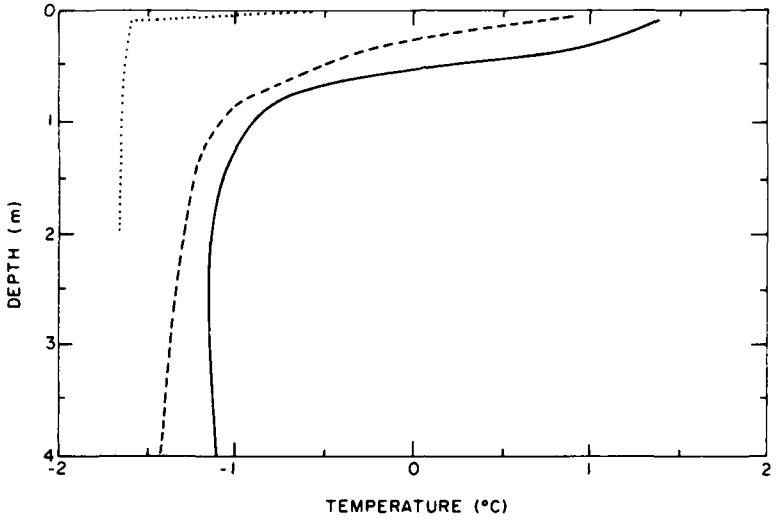

Fig. 8. Comparison of temperature profiles taken at the locations described in Figure 7.

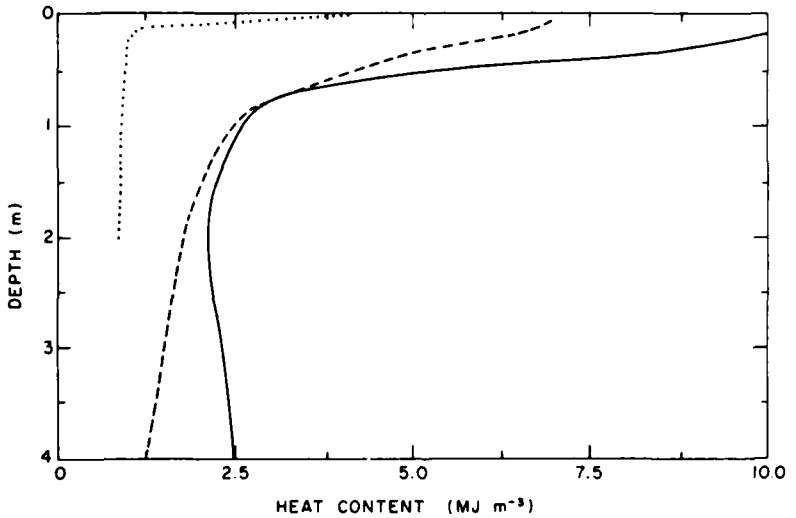

Fig. 9. Vertical variations of heat content in the leads described in Figure 7. Total heat content in the upper 2 m of the water column was 2.0 MJ m^{-2} at Site A, 6.5 MJ m^{-2} at Site B, and 8.6 MJ m^{-2} at Site C.

scattered floes 5–15 m in diameter with open water areas only 3–4 m across. Ice concentration was much lower (perhaps only 50%), but the area was 15–20 km away from open water. There was typically a strong density gradient in the upper 70–100 cm due to meltwater input, but salinities were usually above 15‰, suggesting significant vertical mixing. Salinities below 1 m were generally a few parts per thousand lower than interior values, presumably reflecting the entrainment of surface meltwater. Heat content in the upper 2 m was 2–3 times larger (depending on the distance from an ice wall) than at the interior site. The reason for the greater heat content was probably the greater amount of open water, although there could also be differences in the incident shortwave radiation. Three profiles were taken on 22 July across a 50-m-wide lead. Heat content was substantially larger than in the small leads sampled the previous day and about 4 times as large as the interior site, indicating that both lead size and ice concentration affect the heat content. There was also evidence of more rapid vertical mixing, probably due either to windier conditions or to greater relative motion between the floes. While heat content in the upper 50 cm was roughly constant across the lead, there was about 25% less heat in the water column on the downwind side of the lead. Slightly lower salinity in the water column on the downwind side suggests that the reason for the lower heat content was more efficient transfer of heat to the floe edge, which accelerated the melting.

Radiation measurements

Incoming shortwave and longwave radiation were sampled at Tent Floe every 10 minutes throughout the drift (Figures 10 and 11). Hourly totals are presented in Tables 5 and 6. Shortwave fluxes clearly show the effects of variations in cloudiness superimposed on the diurnal fluctuations. On clear days such as 1 and 3 July, peak shortwave fluxes were about 70% larger than on cloudy days. Figure 10 indicates that cloud cover tended to be thinner at night, even when there was a heavy overcast during the daytime. The diurnal signal in the longwave radiation was weak and the variability seen in Figure 11 is primarily the result of changing cloud conditions. The minima in the curve correspond to clear sky periods. Because of the large amount of water vapor in the air, even in the absence of clouds, fluctuations in incident longwave radiation were only on the order of 30%, considerably smaller than the cloud effects evident on incident shortwave radiation.

Incident spectral irradiances were measured periodically for different degrees of cloudiness. Examples of spectra obtained under clear and cloudy skies near local noon are shown in Figure 12. Maxima and minima seen in the two curves correspond to minima and maxima in the absorption spectra of atmospheric water vapor. The reduction in incoming solar radiation by typical MIZ clouds was roughly a factor of 0.6 in the visible and up to a factor of 3 in the infrared. In addition to observations at the drifting station, spectral data were

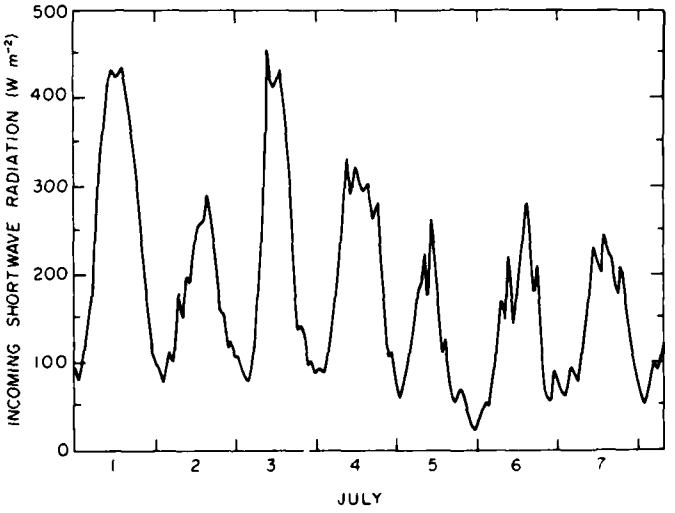

Fig. 10. Incoming shortwave radiation over Tent Floe during the drift phase.

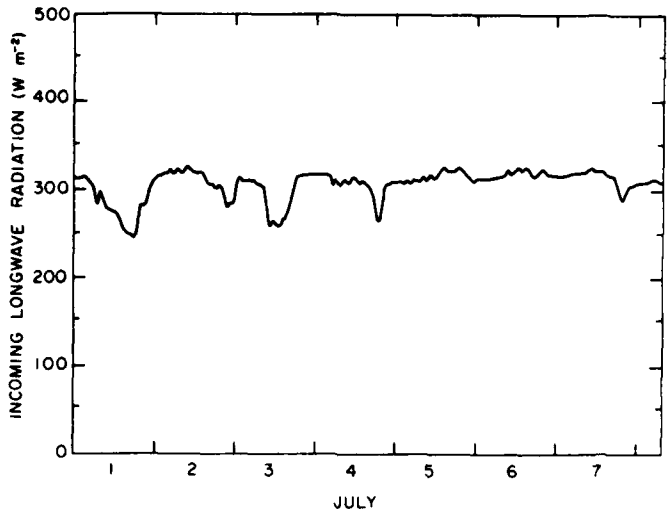

Fig. 11. Incoming longwave radiation over Tent Floe during the drift phase.

Table 5. Hourly totals of incoming shortwave radiation (W/m²) measured over Tent Floe during the drift phase.

	June	July							
Hour (NST)	30	1	2	3	4	5	6	7	8
0100		79	93	92	91	75	47	63	51
0200		94	78	84	87	86	54	78	64
0300		127	95	81	113	104	50	91	87
0400		162	109	98	131	132	83	91	98
0500		178	102	117	155	143	94	75	91
0600		232	116	150	206	184	134	88	100
0700		276	180	208	236	191	171	142	126
0800		343	149	273	290	224	146	146	
0900		359	194	455	329	175	217	183	
1000		414	190	420	290	261	142	228	
1100		430	209	412	320	207	175	217	
1200		427	242	420	318	160	235	200	
1300		425	257	433	295	110	256	244	
1400		433	259	406	293	127	280	222	
1500		419	287	376	302	81	227	219	
1600	163	386	271	306	262	59	177	185	
1700	174	348	239	217	266	54	206	177	
1800	144	315	212	136	280	65	144	207	
1900	124	259	159	141	213	68	67	191	
2000	121	191	154	135	135	51	57	157	
2100	99	175	119	97	109	41	57	114	
2200	86	125	122	102	110	26	87	97	
2300	82	106	108	87	91	21	79	81	
2400	92	97	109	93	61	37	70	58	

Table 6. Hourly totals of incoming longwave radiation (W/m^2) measured over Tent Floe during the drift phase.

	June	July							
Hour (NST)	30	1	2	3	4	5	6	7	8
0100		313	313	313	315	311	313	317	309
0200		313	315	311	315	309	313	315	309
0300		315	317	311	315	311	313	319	311
0400		313	319	311	315	309	313	319	313
0500		309	322	311	306	311	317	319	313
0600		306	319	309	311	311	317	319	309
0700		287	322	304	304	311	317	319	309
0800		295	319	304	309	313	317	319	
0900		287	322	269	311	311	322	324	
1000		276	324	260	309	315	319	324	
1100		276	322	263	313	313	322	322	
1200		274	319	261	313	317	324	322	
1300		274	319	261	309	322	322	322	
1400		258	319	267	311	326	324	319	
1500		254	311	267	306	322	324	317	
1600	317	249	306	289	304	322	317	315	
1700	317	247	304	306	293	322	315	313	
1800	317	245	302	317	265	326	319	293	
1900	315	258	304	317	269	324	324	289	
2000	317	282	302	315	306	319	322	293	
2100	315	282	282	317	306	315	317	306	
2200	315	293	287	317	309	313	317	306	
2300	315	306	287	315	311	311	315	306	
2400	313	311	309	315	311	313	317	309	

gathered onboard the *Polarstern* during its cruise to the Greenland coast. The data showed an even greater reduction in incoming solar radiation under cloudy skies, which appeared to be the result of lower surface albedos and reduced backscattering.

Spectral and total albedos were measured over all available surface types: snow-covered ice, thick and thin first-year ice, multiyear ice, and ponded ice. Examples for snow and thin (75 cm), melting first-year ice are shown in Figure 13. The upper curve in Figure 13 is very similar to previous data

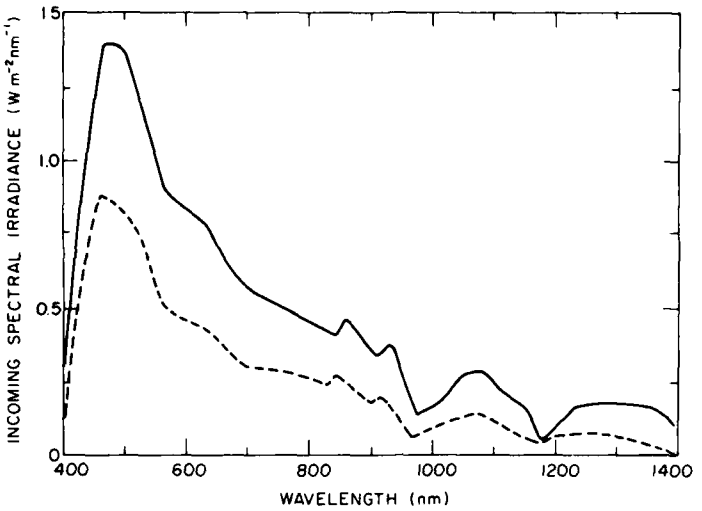

Fig. 12. Incoming spectral irradiance under clear sky conditions (solid curve) on 3 July and under cloudy conditions (dashed curve) on 7 July.

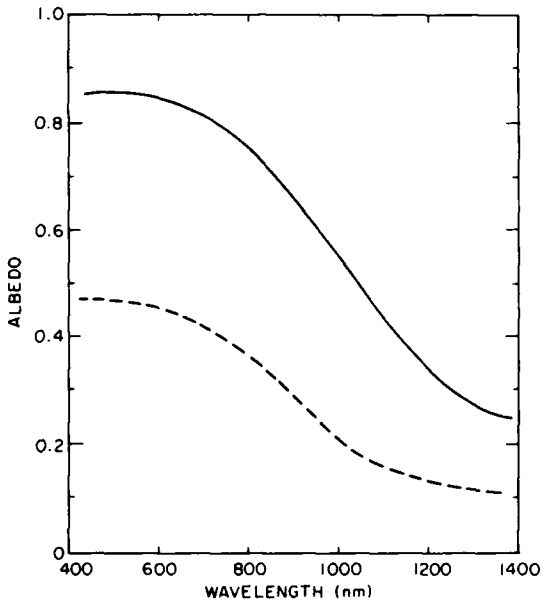

Fig. 13. Spectral albedos observed near the drift station. The solid curve is for a 10-cm-thick snow cover over first-year ice under clear skies on 3 July; the dashed curve is for melting first-year ice, 75 cm in thickness, under cloudy skies on 7 July.

we acquired in the Pt. Barrow area over snow-covered ice in the initial stages of melting. The depression of the albedo below 0.9 in the 500-nm region suggests the presence of some contamination such as soot or dirt in the snow layer. The values for the thin first-year ice do not, however, resemble any of the cases we have previously studied. The decrease in albedo with wavelength is very similar to that of cold, bare ice, but the values are about 0.1 lower. Albedos measured over the more common blue ice are comparable with the thin ice values in the 400–500-nm region, but are much lower in the near infrared. It is believed that this thin ice was very young (2–3 months) and that the difference in optical properties was related to higher salinity in the ice.

ACKNOWEDGMENTS

Radiation data were taken by T. Grenfell, mass balance data by A. Hanson, and CTD data in the leads by J. Morison. The work was made possible by support from the Office of Naval Research under contracts N00014-83-K-0115 and N00014-84-C-0111.

Ocean Currents and Temperatures in the Center of Fram Strait During MIZEX 83

KENNETH HUNKINS
Lamont-Doherty Geological Observatory of Columbia University
Palisades, New York 10964

An array of moored oceanographic recording instruments was placed in Fram Strait at the beginning of the Marginal Ice Zone Experiment in 1983 (MIZEX 83) and recovered at the end of the experiment. The array was situated near the center of the Strait on the sill separating the Arctic Ocean from the Greenland Sea (Figure 1). Three moorings were arranged in a triangle with the fourth mooring at the center of the triangle. Nominal spacing was 10 km, a distance chosen as close to the Rossby radius of deformation in the region. The array was in open water east of the ice edge.

The objective was to monitor mesoscale oceanographic fluctuations in open water near the ice edge. An oceanographic front is generally associated with the ice edge, and two extreme hypotheses might be postulated about mesoscale motion in the area. Such motions could be due to a spectral cascade of energy generated in boundary layers by the mean flow. In this case, spectra in the time domain would be expected to show a monotonic decrease in energy from low to high frequencies, representing a cascade of geostrophic turbulence. An alternate hypothesis would be that instability processes in the mean shear across the front favor the growth of certain discrete frequencies and wavenumbers. In this case the recordings would be expected to show one or more spectral peaks in the subinertial frequency range.

Four subsurface moorings were deployed in water depths of about 2400 m on 16–17 June, 1983, from M/V *Polarbjørn* in an array nominally centered at 78°30'N, 2°E (Table 1). The array location was south of the Molloy Deep, where depths exceed 4000 m, and north of a northwest-southeast trending ridge that rises to a depth of about 1700 m. Bottom slopes were gentle in the area of the array. All of the moorings and instruments were retrieved 41 days later on 27 July, 1983. One of the moorings was then redeployed to record over the next year. It will be retrieved during MIZEX 84. Aanderaa RCM-5 current meters were used to record current speed and direction, as well as temperature and depth. Manufacturer's specifications for these CTD instruments are:

Temperature resolution	±0.01°C
Current speed accuracy	±2% of actual speed
Current direction resolution	±0.35°

Table 1. Mooring locations and depths.

Mooring number	Ocean depth (m)	Latitude N deg	Latitude N min	Longitude E deg	Longitude E min	Aanderaa S.N.	Minimum depth (m)	Mean depth (m)	Maximum depth (m)	Record length (days)
1	2340	78	30.42	1	57.66	5786	52	55	77	26.14
						5461	151	154	179	33.63
2	2347	78	33.78	1	58.80	5378	61	63	92	41.24
						6538	1015	1018	1047	41.15
4	2439	78	36.06	1	52.02	5785	55	59	106	40.78
						5760	158	161	207	40.75
						6536	1014	1017	1059	40.76
						5889	2296	2304	2309	40.74

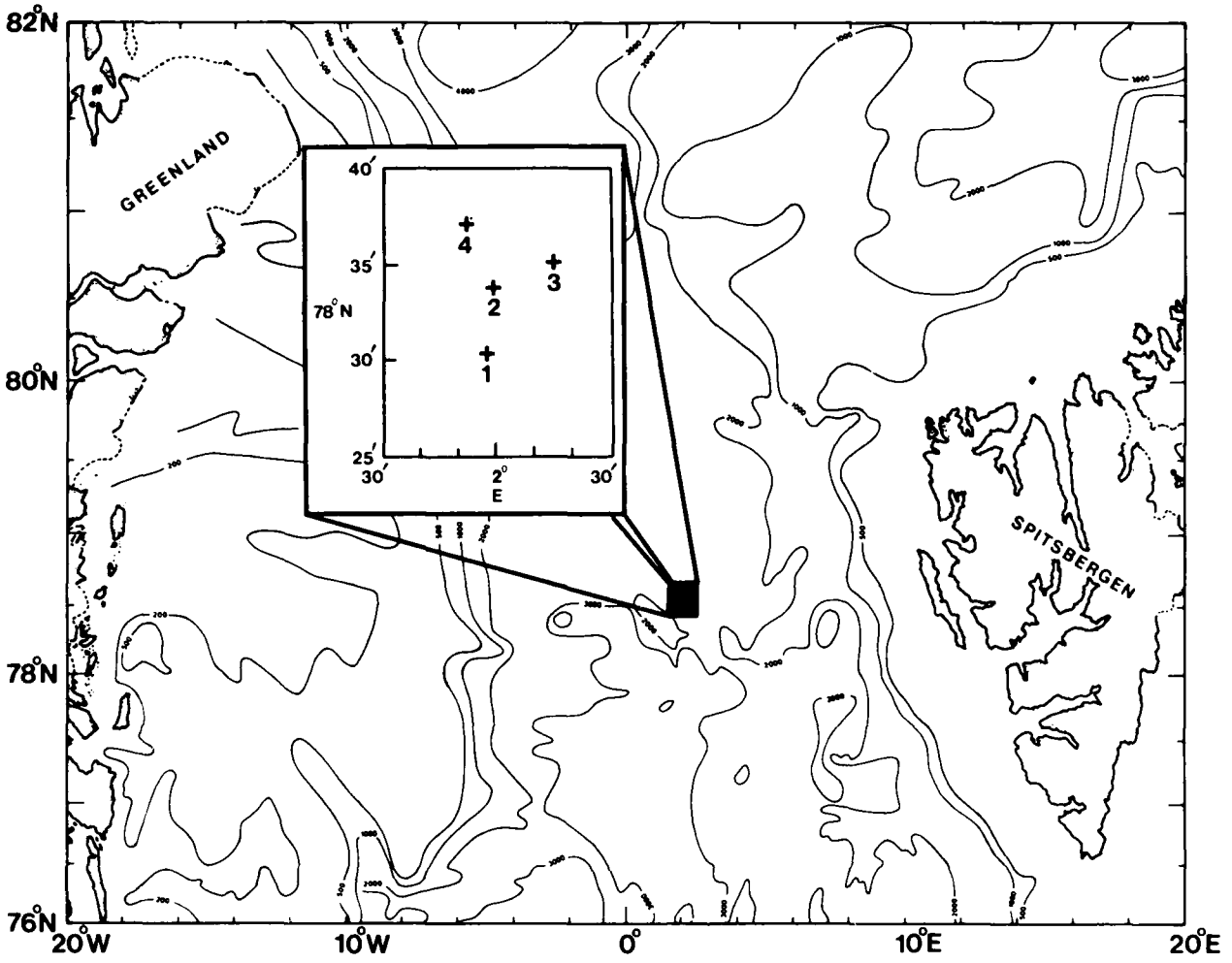

Fig. 1. Location of MIZEX 83 mooring array. (Bathymetry from Johannessen and Johannessen, 1983.)

All instruments were calibrated before the MIZEX 83 cruise. Although the instruments were equipped with conductivity sensors, range settings were incorrect for this region and no salinity data were obtained. Current meters were suspended at nominal depths of 50 and 150 m below the surface on all four moorings. Additional instruments were suspended at depths of 1000 m below the surface and 100 m above the bottom. Data were sampled every 10 minutes.

The magnetic recording tape failed to transport on four of the twelve instruments deployed. The malfunction was later found to be caused by excessive use of tape head cleaner, which did not entirely evaporate before the tape was mounted. This resulted in adhesion of tape to the tape head. Another instrument was accidentally fouled in the mooring cable during launching so that it was unable to swivel. Temperature data are available for that instrument, but current data are invalid. On three other instruments digital noise, apparently due to poor functioning of the digitization mechanism in these three meters, reduced the length of useable record.

The moorings were situated in open water 50 km east of the ice edge, which trends nearly north and south in this region. An oceanographic profile was made from M/V *Polarbjørn* by the University of Bergen Oceanographic Group, with a Neil-Brown CTD instrument, just before the moorings were retrieved (Figure 2). Sigma-*t* was about 27.2 at the surface and increased rapidly with depth in the upper 100 m so that at 150 m it was about 27.8. Below 100 m it increased slowly and was still less than 28.0 at 2000 m. There was a thin layer of warm surface water at about 5 °C that extended to

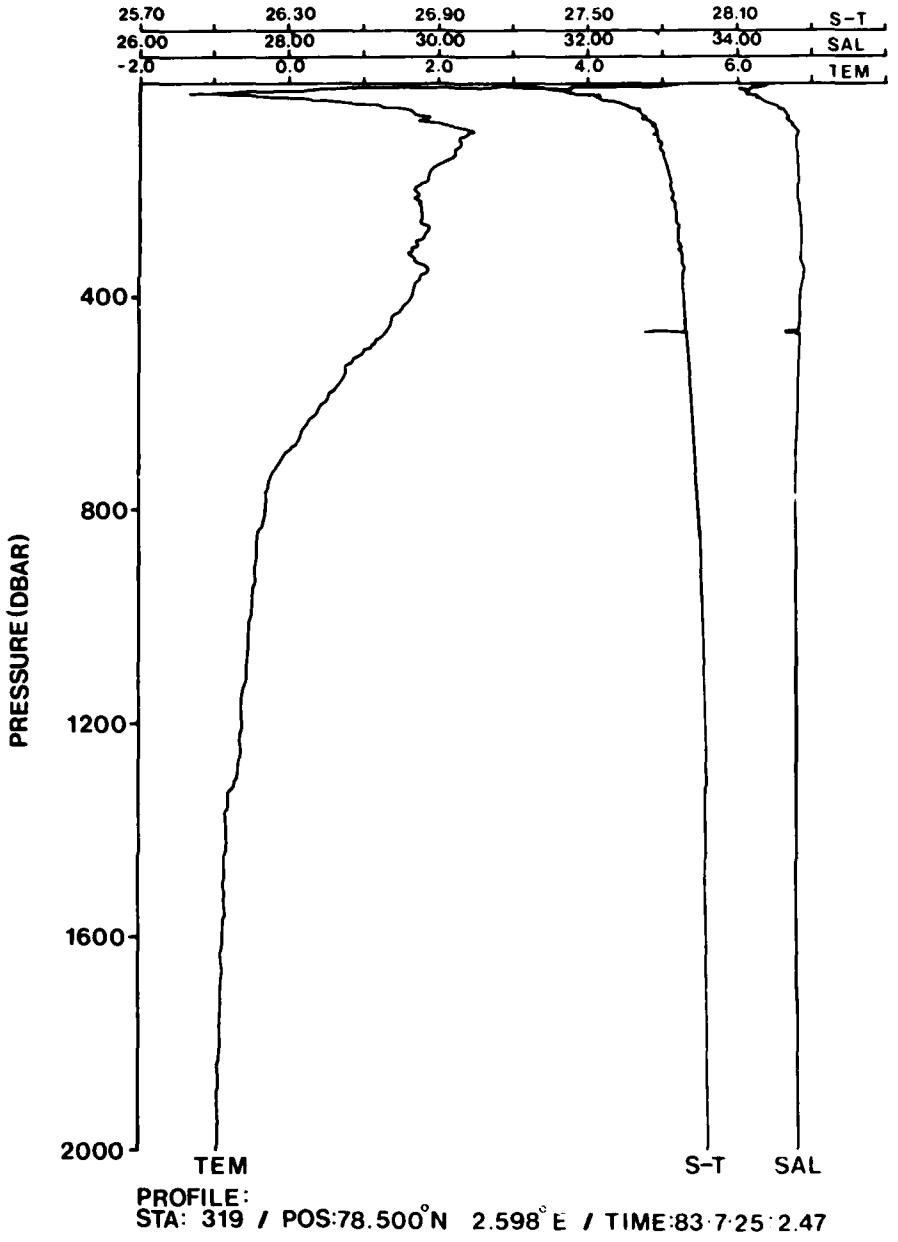

Fig. 2. CTD station 319, 78.5°N, 2.6°E; 25 July 1983. (Redrawn from Johannessen and Johannessen, 1983.)

a depth of only about 10 m. A thin cold layer at 25 m separated the surface layer from a warmer layer of Atlantic origin with maximum temperatures exceeding 2 °C. This layer extended to a depth of 700 m, below which temperatures were negative, closely approaching -1.0 °C at 2000 m. At the surface, salinity was about 34.0 ppt. It increased rapidly with depth in the first 100 m, then increased only slowly at greater depths, approaching a value slightly less than 35.0 ppt at 2000 m.

Mean values and standard deviations for temperature and current components are presented in Table 2. The shallowest instruments, nominal depth of 50 m, had mean temperatures of 3.62, 2.51, and 2.56 °C. The 3.62 °C value is from a shorter record and thus cannot be compared di-

Table 2. Mean values and standard deviations for temperature and current.

Mooring number	*Instrument depth (m)*	*Record length (days)*	$\bar{T}$ *(°C)*	$\bar{u}$ *(cm/s)*	$\bar{v}$ *(cm/s)*
1	52	26	3.62 ±0.56	−1.7 ±8.2	0.4 ±9.4
	151	29	1.67 ±0.30	1.6 ±5.3	−5.0 ±7.3
2	61	41	2.51 ±0.36	—	—
	1015	41	−0.77 ±0.08	1.1 ±2.5	−4.4 ±4.2
4	55	41	2.56 ±0.63	−2.0 ±6.6	−7.5 ±8.2
	158	30	1.62 ±0.40	−2.0 ±5.8	−6.5 ±7.3
	1014	41	−0.74 ±0.08	0.5 ±2.4	−5.2 ±3.8
	2296	41	−1.00 ±0.04	1.2 ±3.0	−7.5 ±3.9

rectly with the other two means of 2.51 and 2.56 °C, which are satisfyingly close to each other in value. Their large standard deviations, ±0.36 and ±0.63 °C, reflect the fact that these instruments are located in a thermocline, so that any vertical water motions produce large recorded temperature variations.

The two instruments at the 150-m level recorded mean temperatures of 1.67 and 1.62 °C, again relatively close in value, as are also the two means of -0.77 and -0.74 °C at the 1000-m level. There was only one record from 100 m above the bottom and the mean at that level was -1.0 °C, quite close to the temperature at 2000 m observed for the CTD profile. The standard deviation of ±0.04 °C near the bottom indicates the constancy of temperature at that level and also gives some measure of the repeatability of the temperature measurements.

Mean curents at four levels in the water column from near the surface to near the bottom all have a southward component (Figure 3). Mean speeds are relatively high, ranging from 5.2 to 7.6 cm/s. Although there are shears between the different levels, it is perhaps the agreement rather than the differences between these means that should be emphasized. The general similarity in speed and direction between the different levels suggests that the mean flow has a large barotropic component. The time series do show some long-period trends extending over several weeks, and means over longer periods might have shown different results. The results do indicate that there must have been a large northward flow in another part of the Strait during this period to compensate for the large observed southward transport.

The MIZEX 83 mooring results represent the combined efforts of many people. The moorings were deployed under the supervision of Ivars Bitte. Jay Ardai, Barry Allen, and Peter Bruchhausen assisted with the launching. Recovery was

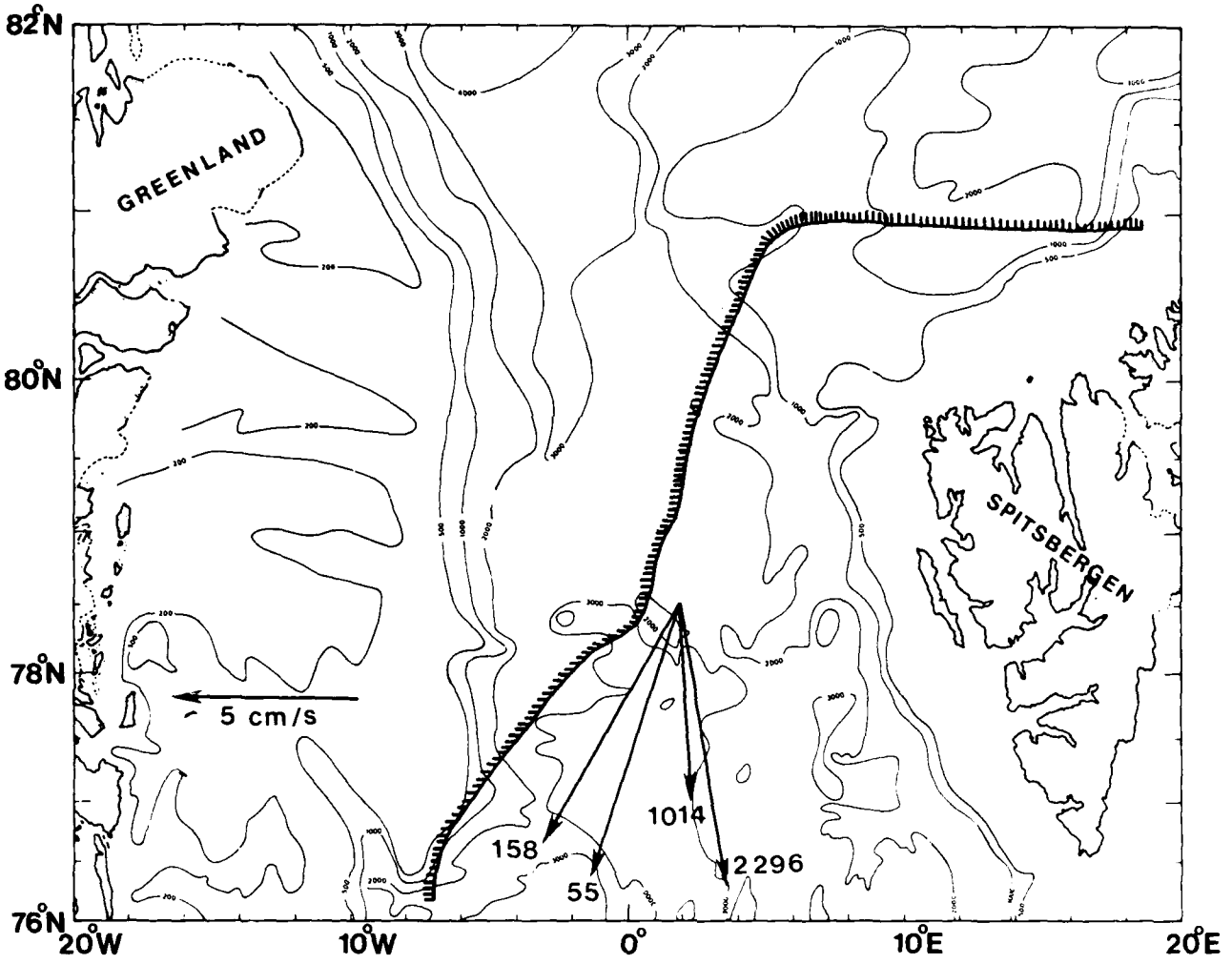

Fig. 3. Mean current vectors at Mooring 4. Depths in meters. 41-day means, except for the 158-m record, which is a 30-day mean.

supervised by Jay Ardai with the assistance of Allan Heilscher. The captain and crew of the M/V *Polarbjørn* provided capable assistance throughout the mooring operations.

Werner Tiemann, Dennis Camp, Barry Allen, and Rich Cember assisted with data reduction. Tom Manley wrote a number of the computer programs used in reduction.

The Lamont Arctic Program is funded by the Office of Naval Research under Contract No. CU-002-97201.

REFERENCE

Johannessen, J.A. and O.M. Johannessen, A CTD report from Marginal Ice Zone Experiment (MIZEX) in the Fram Strait region in June-August 1983, Vol. II. Geophysical Institute, Division A; University of Bergen, Bergen, Norway, 1983.

Arctic Whitecapping: Preliminary Results

E.C. MONAHAN AND P.A. BOWYER
University College, Galway
Republic of Ireland

Our motive for recording whitecap coverage of the sea at high latitudes, and particularly in the vicinity of the ice pack during MIZEX 83, was to extend the sea-water temperature (T_w) range represented in our whitecap (W), windspeed (U) data file so that we could, by application of a suitable statistical methodology (e.g. O'Muircheartaigh and Monahan, 1983a), obtain an improved $W(U, T_w)$ expression. Our hypothesis when we undertook this study to determine the influence on W of T_w, as distinct from the influence of atmospheric thermal stability or the stability-related measure $T_a - T_w$ (where T_a is the air temperature), was that W would decrease with increasing T_w. This hypothesis was based on the following assumptions:

1) For a given wind speed (and stability), that a uniform number of waves would break per unit area of sea surface per unit time, regardless of T_w;

2) That, for any T_w, the average breaking wave would entrain the same amount of air to the same depth; and

3)That the bubble spectrum resulting from wave breaking would be independent of T_w.

When assumptions 2 and 3 are combined with Blanchard's early observations (personal communication), which showed that for any given bubble size the rise velocity of the bubble increases significantly when there is a modest increase in T_w, the conclusion is reached that cold-water whitecaps persist longer than warm-water ones, since the whitecaps in cold water are replenished by bubbles from below for a longer period than are whitecaps in warm water. This conclusion, when taken together with assumptions 1 and 2, leads directly to the aforementioned hypothesis.

We now have at hand the first, preliminary results from the analysis of some of the MIZEX 83 whitecap photographs. While the preliminary results shown in Figure 1 are based on the work of only one analyst and ignore the influence of stability and fetch, they have already, when considered in conjunction with some of our recent whitecap simulation tank findings, caused us to revise our working hypothesis drastically. When the points on Figure 1 are compared with the solid $W(U)$ curve (Monahan and O'Muircheartaigh, 1980) based on warm ocean observations reported in Toba and Chaen (1973) and Monahan (1971), or with the dashed curve (O'Muircheartaigh and Monahan, 1983b, Eq. 9) based on the relatively cool-water (12.5 °–14 °C) JASIN whitecap observations (Monahan et al., 1981), the suggestion arises that for a given U, W is less for cold seas than for warmer waters. Indeed, these preliminary MIZEX 83 low W results are reminiscent of the fresh-water whitecap observations reported by Monahan (1969), even to the relatively high wind speed for the onset of whitecapping—the Beaufort velocity discussed in O'Muircheartaigh and Monahan (1983b).

While these surprising initial MIZEX results were coming to light, some equally intriguing results were being obtained with the U.C.G. whitecap simulation tank. The amount of space charge produced during the decay of the whitecap formed by a 'standard' breaking wave in the tank was found to increase several fold as the temperature of the sea water in the tank was increased from 5 ° to 25 °C (see Figure 5, Bowyer, 1983). This finding lent itself to one of two explanations: either the space charge per aerosol droplet increases markedly with increases in T_w, or the number of droplets (particularly jet droplets in this context) produced per whitecap increases significantly with elevation of T_w. Subsequent experiments, in which a Royco Model 225/241 aerosol particle counter was used to measure the number of droplets injected into the hood of the tank as a result of 'standard' breaking waves produced at various T_w's, showed that the actual number of jet droplets produced per breaking wave increases markedly with increasing T_w. While it has not yet been confirmed

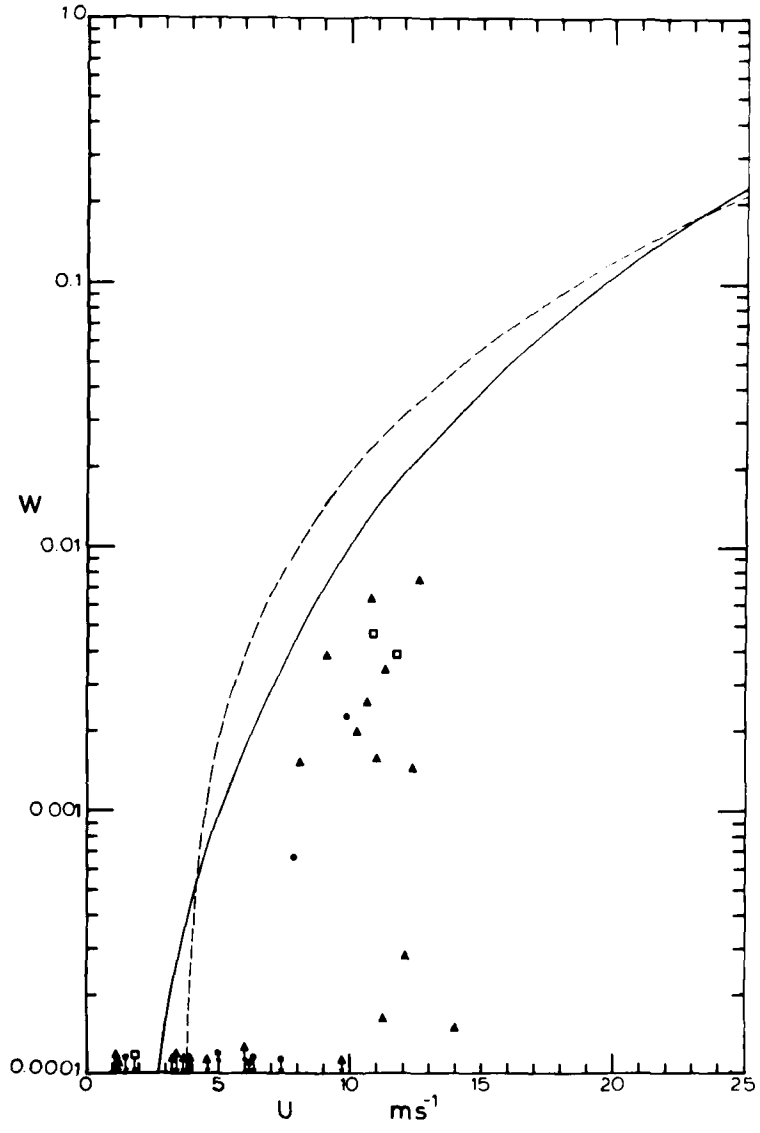

Fig. 1. The fraction of the sea surface covered by whitecaps, W, *vs the wind speed at 10 m elevation,* U; *preliminary results of MIZEX 83 observations. Open squares 12.5°C* $< T_w \leq$ *14°C; filled triangles 5.0°C* $< T_w \leq$ *12.5°C; filled circles* $T_w \leq$ *5.0°C. Each point is based on the analysis of 8 to 22 photographs. This preliminary figure based on the analysis of 346 photographs out of some 1040 taken from F/S* Polarstern. *The solid and dashed curves are described in the text. N.B. Points near bottom of panel with downward pointing arrows have* W *values less than 0.0001. Many correspond to intervals with no whitecaps.*

experimentally, it is probable that this increase in jet droplet production with increasing T_w is due to the fact that, as T_w increases, the number of bubbles increases and the bubble size spectrum peak shifts to smaller bubble radius, probably as a result of reduced viscosity (smaller bubbles are much more efficient generators of jet droplets, as was shown by Blanchard, 1963).

If this interpretation of the tank results is correct, then assumption 3 (and perhaps also assumption 2) listed above is wrong. We thus are left with a new working hypothesis: that cold-water whitecaps persist for briefer periods of time than warm-water whitecaps because, in spite of the greater viscosity of the cold water, the larger bubbles that replenish the cold-water whitecaps reach the surface sooner than the small bubbles that sustain warm-water whitecaps. A concomitant of this hypothesis is that for the same U, W is less in cold seas than in warm. Indeed, this argument is essentially the same, with regard to the effect of bubble spectra on $W(U)$, as that put forth to explain the relatively low W values observed on the North American Great Lakes as compared to those obtained from oceanic observations (Monahan and Zietlow, 1969; Monahan, 1971).

We hope shortly to use a video area analyzer in conjunction with our MIZEX 83 whitecap tapes to test this new hypothesis as regards the short lifetimes of cold-sea whitecaps. We look forward to collecting additional video and photographic records during MIZEX 84 that will enable us to refine the $W(U,T_w)$ expression that we will initially base on the MIZEX 83, STREX (Doyle, 1984), JASIN, and BOMEX whitecap observations. The resulting $W(U,T_w)$ expression can then be introduced into our sea surface aerosol generation model (Monahan et al., 1982, 1983a), and the improved model can be used to obtain revised estimates of global sea-to-air salt fluxes.

The research discussed in this note is sponsored by the U.S. Office of Naval Research via grant N00014-78-G-0052. The MIZEX 83 whitecap observations were recorded aboard the F/S *Polarstern* of the Alfred Wegener Institut, Bremerhaven. The assistance of Prof. E. Augstein, the other scientists, and the crew of the *Polarstern* is gratefully acknowledged. The whitecap results presented in Figure 1 are based on the photographic analyses of Miss M. Higgins. The extrapolation of the winds to 10-m elevation values was done by Dr. M.C. Spillane.

REFERENCES

Blanchard, D.C., The electrification of the atmosphere by particles from bubbles in the sea, *Prog. in Oceanog., 1,* 71–202, 1963.

Bowyer, P.A., New estimate of the space charge produced in the laboratory, pp. 60–77, (Chapter 5) in Monahan et al., 1983b.

Doyle, D.M., M.Sc. thesis, Dept. of Oceanography, University College, Galway (in prep.), 1984.

Monahan, E.C., Fresh water whitecaps, *J. of Atmos. Sci., 26,* 1026–1029, 1969.

Monahan, E.C., Oceanic white-caps, *J. of Phys. Oceanogr., 1,* 139–144.

Monahan, E.C. and I.G. O'Muircheartaigh, Optimal power-law description of oceanic whitecap coverage dependence on wind speed, *J. of Phys. Oceanogr., 10,* 2094–2099, 1980.

Monahan, E.C., and C.R. Zietlow, Laboratory comparisons of fresh-water and salt-water whitecaps, *J. of Geophys. Res., 74,* 6961–6966, 1969.

Monahan, E.C., K.L. Davidson, and D.E. Spiel, Whitecap aerosol productivity deduced from simulation tank measurements, *J. of Geophys. Res., 87,* 8898–8904, 1982.

Monahan, E.C., I.G. O'Muircheartaigh, and M.P. FitzGerald, Determination of surface wind speed from remotely measured whitecap coverage, a feasibility assessment, *Proceedings of an EARSel-ESA Symposium,* Application of Remote Sensing Data on the Continental Shelf, Voss, Norway, 19–20 May, European Space Agency SP-167, 103–109, 1981.

Monahan, E.C., D.W. Spiel, and K.L. Davisdon, Model of marine aerosol generation via whitecaps and wave disruption, Ninth Conference on Aerospace and Aeronautical Meteorology, 6–9 June 1983, Omaha, Nebraska, American Meteorological Society, Preprint Volume, 147–158, 1983a.

Monahan, E.C., M.C. Spillane, P.A. Bowyer, D.M. Doyle, and P.J. Stabeno, Whitecaps and the Marine Atmosphere, Report No. 5 to the Office of Naval Research, from University College, Galway, 1–93, 1983b.

O'Muircheartaigh, I.G., and E.C. Monahan, Use of the Box-Cox transformation in determining the functional form of the dependence of oceanic whitecap coverage on several environmental factors, Preprint volume, Eighth Conference on Probability and Statistics in Atmospheric Scienc-

es, 16–18 November, Hot Springs, Arkansas, 3.5, 55–58, 1983a.

O'Muircheartaigh, I.G. and E.C. Monahan, Aspects of oceanic whitecap coverage dependence on wind speed; heteroscedasticity in the data, and the estimation of the Beaufort velocity, Preprint volume, Second International Meeting on Statistical Climatology, 26–30 Sept, Lisbon, Portugal (2.7. 1–4), 1983b.

Toba, Y., and M. Chaen, Quantitative expression of the breaking of wind waves on the sea surface, *Rec. of Oceanogr. Works in Japan, 12,* 1–11, 1973.

END

FILMED

1-85

DTIC